2

Design and Fabrication of Flexible Piezoelectric Generators Based on ZnO Thin Films

2.1 Introduction

The study of energy has recently been gaining more attention. Various clean, green, and renewable energy systems have been extensively developed and explored to help address the problem of energy shortage. Alternative energy systems have been actively researched worldwide while regarding considerations such as compact size, light weight, high density in power, economy, safety, and environmental concerns. The numerous renewable sources of green energy include hydroelectric [1], wind [2], oceanic [3], solar [4–6], and vibration [7, 8]. However, environmental constraints generally limit recycling power applications. For instance, hydroelectric power plants are always built with turbines, such as the Pelton turbine or the chain turbine.

Solar power is the most frequently used energy source. However, applying solar power is restricted by day-and-night limitations [9]. The development of green energy

Design and Fabrication of Self-Powered Micro-Harvesters: Rotating and Vibrating Micro-Power Systems, First Edition.
C. T. Pan, Y. M. Hwang, Liwei Lin and Ying-Chung Chen.
© 2014 John Wiley & Sons Singapore Pte Ltd. Published 2014 by John Wiley & Sons Singapore Pte Ltd.

should therefore address the disadvantages of solar power. In many applications, for example, solar power has been applied in microactuators and microsensors in microelectromechanical systems (MEMS) that require an independent and embedded power source without an outside connection. A possible solution is to design the power supply to the same scale as actuators, sensors, and electronics [10]. The conventional solution involves using batteries however, which can be undesirable for many reasons: they tend to be relatively bulky, contain a finite amount of energy, have a limited life, and contain hazardous chemicals [11].

In many applications, microsystems must be self-powered; efficient energy scavenging is therefore crucial. Mechanical vibration is ubiquitous in real environments. Converting ambient mechanical vibration to electrical energy is considered one of the likely methods for powering wireless sensors without hazardous byproducts related to power generation. In addition, the power source of wireless sensors does not need to be replaced and the fuel does not require periodical replenishment as for batteries [12]. Piezoelectric materials have electrical-mechanical coupling effects, and are the leading candidates for converting mechanical energy into electricity [13]. White *et al*. [14] developed an inertial piezoelectric generator that uses 7-μm-thick film of lead zirconate titanate (PZT) with a 100-μm-thick steel substrate. The device produces an output of 2.1 μW from vibrations in the environment. Roundy *et al*. [15] improved the geometry of the scavenger's piezoelectric bimorph. Using the same volume of PZT and a trapezoidal geometry can supply more than twice the energy of rectangular geometry. Fang *et al*. [16] used a generator structure of a nickel-metal composite cantilever. At a resonant frequency of approximately 608 Hz, 608 mV of AC voltage value with a 2.16 μW power level was obtained. Minazara *et al*. [17] used a mechanically excited unimorph piezoelectric membrane transducer. A power output of 0.65 mW was generated at the resonance frequency (1.71 kHz) across a 5.6 kΩ optimal resistor.

Several harvesting systems of resonant mechanical vibration energy are currently under investigation. Three considerations potentially affect transducer technology selection:

- **Electromagnetic**: a coil attached to a mass that vibrates through a magnetic field to induce voltage according to Faraday's law [18–23].
- **Piezoelectric**: using piezoelectric material to convert strain energy into electricity [9–18, 24–26].
- **Electrostatic**: inducing capacitor voltage through the movement of a mass that has its permanent charges electrically arranged [15, 27].

Dutoit *et al*. [27] compared these three generators according to energy density. Of these three mechanisms, the electrostatic transducer has the lowest energy storage density and conversion efficiency. Further, electromagnetic generators usually require

a large operating space, complex instrumentation, and continual management of facilities, all of which are expensive. Many researchers have therefore examined micropiezoelectric power generators and their fabrication from mostly piezoelectric materials $(Pb,Zr)TiO_3$ (PZT), aluminum nitride (AlN), and zinc oxide (ZnO). Table 2.1 lists the general characteristics and properties of PZT, AlN, and ZnO films [28].

The production of PZT piezoelectric material causes considerable environmental pollution. This study adopted ZnO as a piezoelectric thin film for three main reasons: (1) it has relatively high piezoelectric coefficients compared to piezoelectric AlN [24]; (2) producing ZnO thin film does not cause substantial environmental pollution compared to piezoelectric PZT thin film; and (3) it is a non-ferroelectric material that requires no poling or post-deposition annealing. These factors make ZnO piezoelectric material useful for elucidating the application of piezoelectric energy harvester in environments.

This chapter is organized in four sections to describe the research and developmental efforts. Section 2.1 briefly introduces the background of green and renewable energy systems, the development of generator technologies, and the materials of piezoelectric thin films for piezoelectric generators.

Section 2.2 focuses on the theoretical analysis and simulations of flexible piezoelectric generators based on ZnO thin films on polyethylene terephthalate (PET) substrates. A piezoelectric cantilever plate was designed and simulated using commercial software ANSYS FEA (finite element analysis) to determine the optimal thickness of the PET substrate, internal stress distribution, operation frequency, and electric potential.

Section 2.3 describes the relationship between the model solution of piezoelectric cantilever plate equation, vibration-induced electric potential, and electric power. Section 2.4 discusses the development of high-performance piezoelectric generators using single-sided and double-sided ZnO thin films on a flexible stainless steel substrate (SUS304). Relevant fabrication processes, experiments, measurements, and piezoelectric responses are addressed.

Table 2.1 General characteristics and properties of piezoelectric materials [28]

	Mass density ($kg\,m^{-3}$)	Electromechanical coupling coefficient k_t^2 (%)	Dielectric constant ε_r
PZT	1550	20.25	309.8
ZnO	5680	7.5	8.85
AlN	3270	6	9.14

2.2 Characterization and Theoretical Analysis of Flexible ZnO-Based Piezoelectric Harvesters

2.2.1 Vibration Energy Conversion Model of Film-Based Flexible Piezoelectric Energy Harvester

Figure 2.1a shows the composite cantilever plate used as a harvester with a rectifying circuit (B) and a capacitor (C) as the energy storage module. Ambient vibration amplitude on the anchor side induced vertical deflection at the front end of the cantilever plate. The piezoelectric layer on the composite structure deformed when the cantilever plate oscillated with mass. The bending results in a mechanical strain distributed along the cantilever plate, which is then converted to alternating voltage through the transverse-mode (d_{31}) piezoelectric effect (the generated strain is perpendicular to the electric field, which forms the d_{31} mode of the piezoelectric element), and overcomes the forward bias of the rectifying diodes. Subsequently, the full-wave rectified potential can quickly charge the storage module.

Figure 2.1b shows a schematic model of vibration energy conversion. The mechanical behavior of a vibrating piezoelectric harvester can be modeled using a seismic mass m bonded on a spring k corresponding to the stiffness and a damping factor b_m, which in turns corresponds to the mechanical losses of the structure. A displacement $y(t)$ is used to vibrate the rigid house, resulting in differential movement $x(t)$ between the mass and the house; the relative displacement of the mass is therefore $U_z(t)$.

This section reports the analysis of a new self-powered flexible Cu/ZnO/Al/PET-based piezoelectric energy harvester with a storage module. To verify the optimal thickness of the PET substrate evaluated by performing finite element model (FEM) analysis, an accurate analytical formula was developed. The optimal thickness of the substrate was calculated. Thus, the tensile and compressive strains do not occur

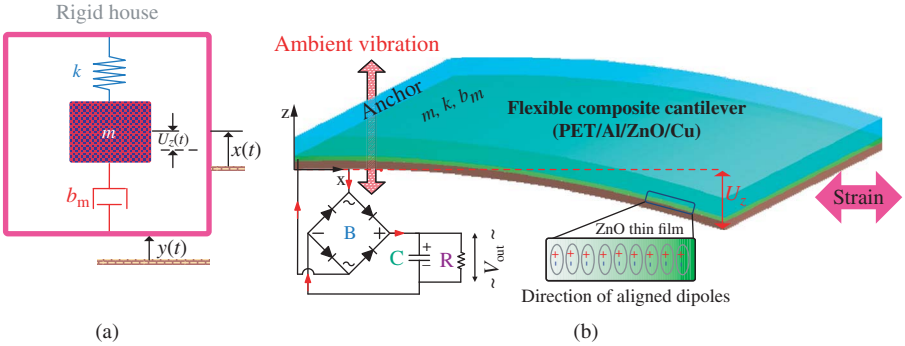

Figure 2.1 Generic vibration energy conversion model: (a) schematic model of flexible piezoelectric cantilever plate according to d_{31} conversion mode and (b) first-order model of a resonant system [28]

on the piezoelectric ZnO layer simultaneously. Static analysis, modal analysis, and harmonic response analysis were performed to determine a suitable thickness of the PET substrate, structural modal parameters, frequency response functions, and electric potential.

In the fabrication process, the piezoelectric ZnO thin film was deposited between the Al and Cu electrodes. The Al thin film used as the bottom electrode was deposited on the PET substrate by using a sputtering deposition method because of its superior adhesion to the PET substrate and lattice constant matching with ZnO. The ZnO thin film with superior compactness and more even distribution of crystal grains with a high (002) diffraction peak at $2\theta = 34.44°$ and full-width at half-maximum (FWHM) of 0.422° was deposited using RF magnetron sputtering. To fabricate the selectively deposited ultraviolet- (UV)-curable resin lump structures as a proof mass, electrospinning and stereolithography techniques were used to construct various patterns on the back of the PET-based piezoelectric composite plate, which can adjust the resonant frequencies of the composite cantilever plate to achieve larger deflection. Piezoelectric ZnO thin-film harvesters can therefore harvest energy in small work spaces. In addition, they demonstrate long-term stability, have a low operating frequency with low-level excitation and a high deflection response compared to traditional PZT-based bulk ceramic vibrational structures, and can be used at low cost in clean energy applications. The schematic layout of the self-powered storage system and the design parameters of the flexible piezoelectric composite plate are shown in Figure 2.2.

In this study, a broad bandwidth harvesting system with a wide bandwidth of 100–400 Hz was designed and fabricated. Four individual, flexible PET-based ZnO piezoelectric harvesters were assembled in parallel with a rectifying circuit

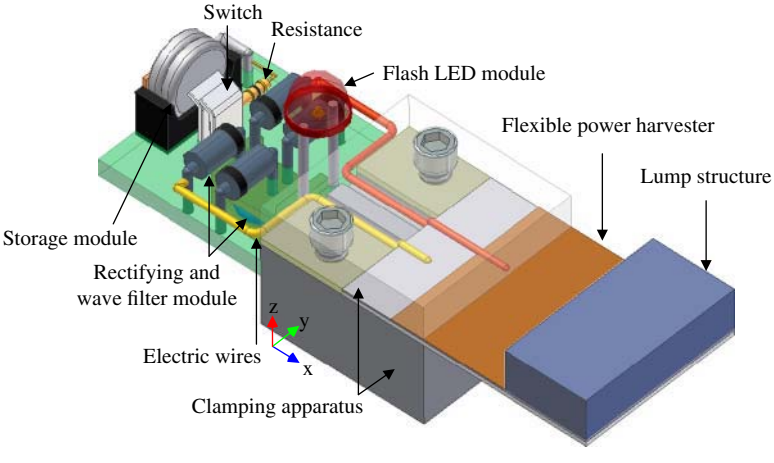

Figure 2.2 Schematic illustration of self-powered storage system and flexible composite structure [28]

and storage module. A schematic illustration of a broad bandwidth piezoelectric harvesting system with the rectifying storage module is shown in Figure 2.3. There are four rectifying circuits in parallel connection and four capacitors are assembled into a storage module [29].

Finally, the effect of vibration on the mechanical and electrical properties of multilayer flexible electronics composites such as ITO (indium tin oxide)/PET, Al/PET, ZnO/ITO/PET, and ZnO/Al/PET was examined to analyze the coating adhesion, mechanical strength, and conductivity. Nanoscratching tests (Nanoindenter XP system) were conducted to examine the adhesion of multilayer interfaces. Field-emission scanning electron microscopy (FE-SEM) and optical microscopy (OM) were employed to observe the surface morphology following the test. In addition, scratching experiments using Berkovich and conical probes on multilayered structures were compared and investigated.

2.2.2 *Piezoelectricity and Polarity Test of Piezoelectric ZnO Thin Film*

Figure 2.4 shows the response of induced electric potential when a periodic force is applied to the piezoelectric cantilever structure (Cu/ZnO/Al/PET). The bending

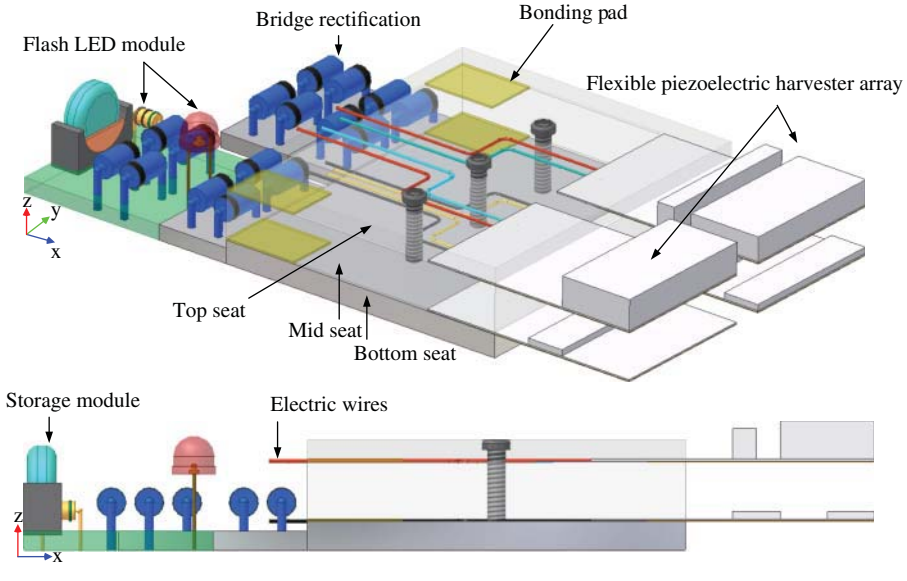

Figure 2.3 Schematic illustration of piezoelectric harvesting system with broad bandwidth [29]

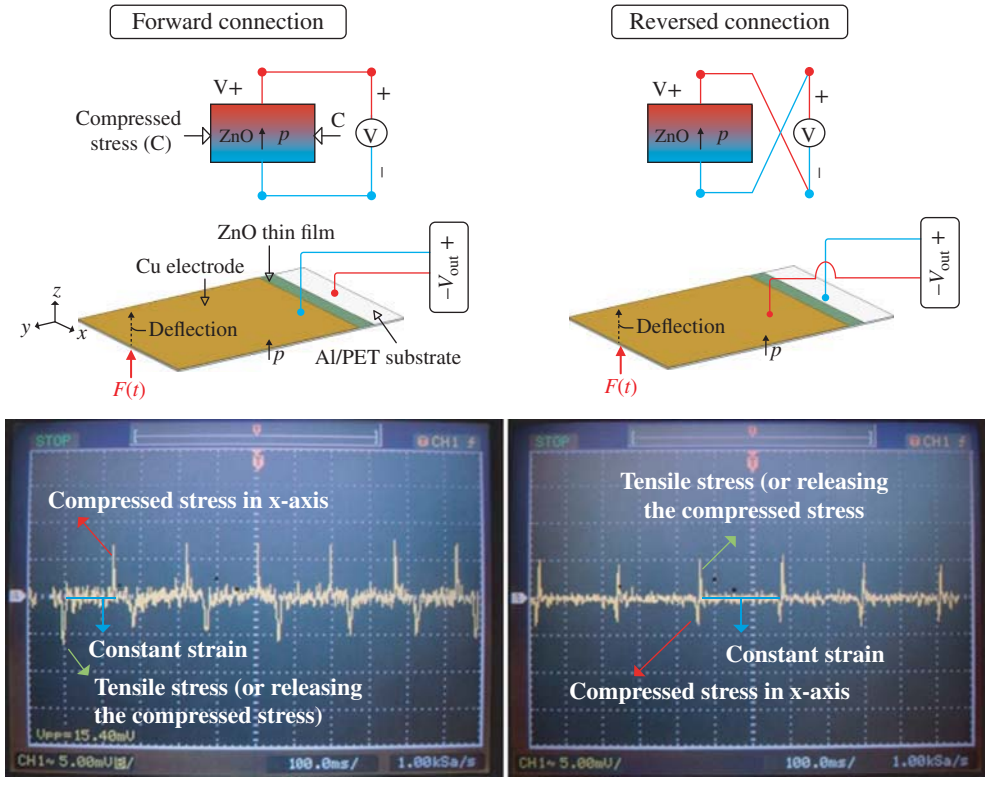

Figure 2.4 Polarity test of piezoelectric ZnO thin film can be observed by piezoelectricity responses: (a) forward-connected to the measurement system and (b) reverse-connected to the measurement system [28]

results in a mechanical strain distributed along the ZnO thin film, which is then converted to alternating voltage through the transverse-mode (d_{31}) piezoelectric effect.

The center of the cations (Zn^{2+}) and the center of the anions (O^{2-}) relatively displaces in the Wurtzite-structured ZnO crystal by applying stress and result in an electric dipole moment (Figure 2.5a). A constructive summation of the dipole moments created by all units in the crystal creates a piezoelectric field (E_z) due to the polarization of atoms, resulting in a macroscopic potential drop between the two sides along the crystal z-axis. This is the piezoelectric potential, or piezopotential, which can serve as the driving force for the flow of electrons in the external load once it is subjected to mechanical deformation, the fundamental working principle of the ZnO film-based energy harvester. Figure 2.5b shows a simplified model of the piezoelectricity of ZnO film. In the absence of external stress, the ionic charge distribution is symmetric and the net electric dipole moment is zero.

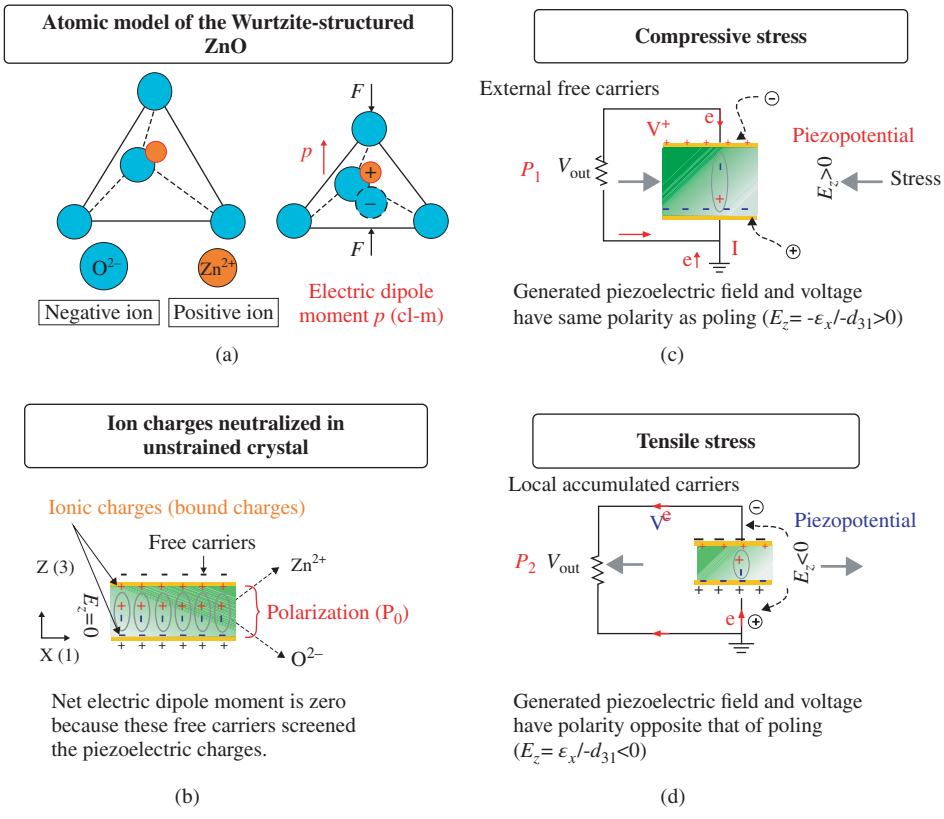

Figure 2.5 Mechanical bending of the substrate creates tensile strain and a corresponding piezoelectric potential in ZnO thin film: (a) atomic model of the wurtzite-structured ZnO; (b) the net electric dipole moment is zero in unstrained ZnO thin film; (c) a compressive stress is applied to the ZnO thin film in x-axis, leading to a drop in the piezoelectric potential along z-axis, and forcing electrons to flow along an external circuit to charge the film; and (d) when the stress is released, electrons flow back in the opposite direction [28]

When compressive stress is applied to the crystal on the *x*-axis (Figure 2.5c), a piezoelectric field ($E_z > 0$) is created in the ZnO film because of the induced ionic charges (or polarization P_1) in the crystal, and induces a higher piezopotential V^+ on the +*c*-axis side. These piezoelectric charges, which are non-mobile, remain in the ZnO thin film for an extended period without being depleted by the free carriers as long as the stress is preserved [30]. Because the charges associated with the ions are rigid and affixed to the atoms, they cannot move freely. The electrons can be driven forward by the positive piezopotential through the external circuit (known as the piezoelectric-potential-driven flow of external electrons), forming the positive potential signal as shown in the red line area of Figure 2.4a. In this study, this process has to be faster than the charge-accumulation process because the external free

carriers are also driven to balance this piezopotential. Under a constant strain, the piezopotential gradually vanished because of a balance between external free carriers and this potential (known as the screening effect of the charge carriers). The piezopotential in piezoelectric materials is therefore a function of the changing stress. As the tensile stress is applied (the compressed stress on the x-axis is released) (Figure 2.5d), the piezopotential V^- reverses with a higher potential at the *c*-axis side. The local accumulated carriers at both ends of the ZnO film quickly flow to the top electrode, creating a circular flow of the electrons in the external circuit and producing a negative signal caused by the reverse-flowing carriers shown in the green line area. This process is considerably faster than the charge-accumulation process. Furthermore, when the harvester is connected in reverse polarity, all of the response signals exhibit reversed output (Figure 2.4b). It is proposed that satisfying the polarity and criteria is a necessary and sufficient condition for confirming that the output is generated by the flexible ZnO energy harvester.

2.2.3 Optimal Thickness of PET Substrate

The neutral axis (NA) position in a composite plate can influence stress distribution [30]. The optimal thickness of a PET substrate is calculated using the geometric parameters on the y–z-plane, as shown in Figure 2.6. The neutral axis position is situated between the PET layer and the Cu foil layer. The desirable thickness of the PET substrate $\bar{t}_{\mathrm{PET}}$ is defined

$$\bar{t}_{\mathrm{PET}} \geq t_{\mathrm{Cu}}\sqrt{\eta_2} \pm 0.5t_{\mathrm{ZnO}} \tag{2.1}$$

where t_i is the thickness of each layer ($i = 1, 2, 3$), η_i is the ratio of the elastic constant and $\eta_1 = E_{\mathrm{ZnO}}/E_{\mathrm{PET}}$ and $\eta_2 = E_{\mathrm{Cu}}/E_{\mathrm{PET}}$, where E_{PET}, E_{ZnO}, and E_{Cu} are the elastic constant of the PET substrate, the ZnO piezoelectric material, and the Cu foil.

In the composite plate, the tensile and compressive strain should not occur on the piezoelectric ZnO layer as the plate experiences a time-varying vibration. By contrast, the one-way mechanical strain is sufficient to enhance the electric charge output, which is generated within the top and bottom electrodes of the ZnO layer.

2.2.4 Model Solution of Cantilever Plate Equation

Figure 2.6 depicts schematic diagrams of the composite cantilever plate with geometric variables. The deflection at each position x of the composite plate is defined by Equation (2.2).

$$U_z(x) = \frac{M(l-x)l^3}{3E_{\mathrm{PET}}Ix} \tag{2.2}$$

where $U_z(x)$ is derived from an equivalent moment $M(l-x) = F_z x$, which is caused by an externally applied force F_z. The maximum vertical deflection at the free end of

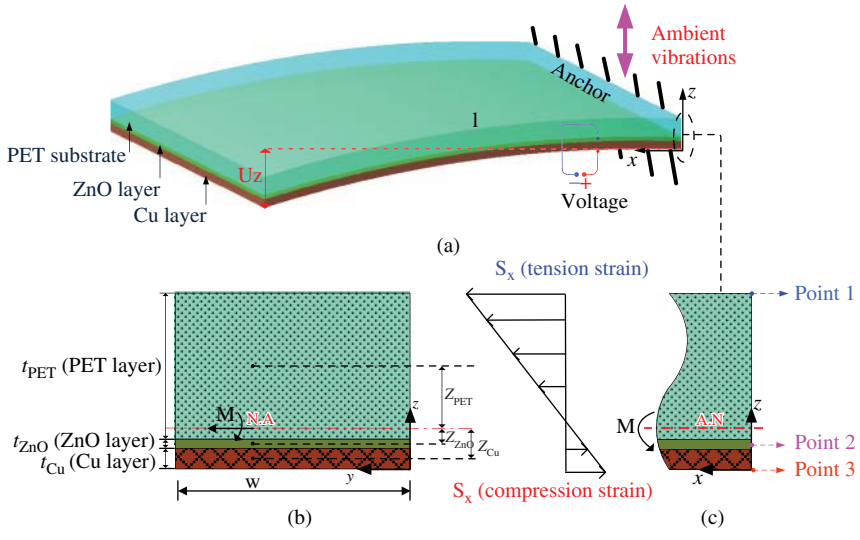

Figure 2.6 Schematic layout of the composite cantilever plate: (a) the deflection (U_z) in the free end of the cantilever, (b) the geometry of ZY plane, and (c) the position of neutral axis and the strain distribution [28]

the cantilever plate is given by Equation (2.3):

$$U_z(l) = \frac{M(0)l^2}{3E_{\text{PET}}I} \tag{2.3}$$

The effective moment of the inertia of the composite plate is developed using Equation 2.4:

$$I = \frac{wt_{\text{PET}}{}^3}{12} + wt_{\text{PET}}z_{\text{PET}}{}^2 + \frac{\eta_1 wt_{\text{ZnO}}{}^3}{12} + \eta_1 wt_{\text{ZnO}}z_{\text{ZnO}}{}^2 + \frac{\eta_2 wt_{\text{Cu}}{}^3}{12} + \eta_2 wt_{\text{Cu}}z_{\text{Cu}}{}^2 \tag{2.4}$$

where z_i is the distance between the center of the geometry and the neutral axis of the three layers (z_{PET}, z_{ZnO}, and z_{Cu}), and w is the width of the plate.

The large deflection theory of thin plate can be employed when the deflection is small relative to the width and length of the plate [31]. The internal strain on the x-axis for a point within the plate can be expressed [32]:

$$S_x = -z\frac{\partial^2 U_z(x)}{\partial x^2} \tag{2.5}$$

The axial strain on the ZnO layer is defined by Equation (2.6).

$$S_{x,\text{ZnO}} = -z_{\text{ZnO}}\frac{\partial^2 U_z(x)}{\partial x^2} \tag{2.6}$$

The distance z is from the neutral axis to each plane within the thickness of the composite plate. The internal stress distribution is related to the ratio of the elastic constant, and the stress in the plate is defined by Equation (2.7) [33]:

$$T_x = -\frac{E}{1-\upsilon} z \frac{\partial^2 U_z(x)}{\partial x^2} \tag{2.7}$$

where υ is Poisson's ratio.

The axial stress on the ZnO layer must be modified according to the ratio of the elastic constant η_1:

$$T_{x,\mathrm{ZnO}} = -\eta_1 \frac{E_{\mathrm{PET}}}{1-\upsilon_{\mathrm{PET}}} z_{\mathrm{ZnO}} \frac{\partial^2 U_z(x)}{\partial x^2} \tag{2.8}$$

The neutral axis $\overline{Z}$ of the composite plate is calculated via:

$$Z = \frac{(wt_{\mathrm{PET}})\left(\frac{t_{\mathrm{PET}}}{2} + t_{\mathrm{ZnO}} + t_{\mathrm{Cu}}\right) + (\eta_1 wt_{\mathrm{ZnO}})\left(\frac{t_{\mathrm{ZnO}}}{2} + t_{\mathrm{Cu}}\right) + (\eta_2 wt_{\mathrm{Cu}})\left(\frac{t_{\mathrm{Cu}}}{2}\right)}{(wt_{\mathrm{PET}}) + (\eta_1 wt_{\mathrm{ZnO}}) + (\eta_2 wt_{\mathrm{Cu}})} \tag{2.9}$$

The maximum axial stress and strain distributed on the ZnO layer are defined by Equations (2.10) and (2.11), respectively:

$$T_{x,\mathrm{ZnO,max}} = \frac{M(0) z_{\mathrm{ZnO}}}{I} = \frac{3\eta_1 E_{\mathrm{PET}} z_{\mathrm{ZnO}} U_z(l)}{l^2} \tag{2.10}$$

$$S_{x,\mathrm{ZnO,max}} = \frac{3(1-\upsilon_{\mathrm{PET}}) z_{\mathrm{ZnO}} U_z(l)}{l^2} \tag{2.11}$$

Improving the axial stress on the ZnO layer is achieved by analysis of these parameters. To obtain the electrical circuit equation with mechanical coupling, the following piezoelectric constitutive relationship should be considered:

$$D_z = d_{31} T_x + \varepsilon_{33}^T E_z \tag{2.12}$$

where D_z is the electric displacement in the direction of the z-axis, d_{31} is the piezoelectric strain coefficient that couples the electric field in the z-axis with the stress T_x, ε_{33}^T is the permittivity at a constant stress, and E_z is the external electric field in the ZnO in terms of the electric potential across the ZnO layer (i.e. $E_z = v/t_{\mathrm{ZnO}}$ where v is electric potential). If Equation (2.12) is rearranged to express the maximum axial stress T_x of the ZnO layer, then the external electric field is assumed to be zero and the electric displacement of the ZnO layer can be expressed:

$$D_z = d_{31} \frac{3\eta_1 E_{\mathrm{PET}} z_{\mathrm{ZnO}} U_z(l)}{l^2} \tag{2.13}$$

The total strain-induced charge Q on the ZnO layer is defined:

$$Q = \int D_z dA = \int_0^l D_z w \, dx = \frac{3\eta_1 E_{\mathrm{PET}} z_{\mathrm{ZnO}} U_z(l) w d_{31}}{l} \tag{2.14}$$

The maximum induced electric potential between the top and bottom surfaces of the ZnO layer is defined:

$$V_{\max} = \frac{Q}{C_{\mathrm{ZnO}}} = \frac{3\eta_1 E_{\mathrm{PET}} z_{\mathrm{ZnO}} U_z(l) t_{\mathrm{ZnO}} d_{31}}{l^2 \varepsilon_{33}} \tag{2.15}$$

where C_{ZnO} and ε_{33} represent the capacitance and the permittivity of the ZnO, respectively.

Detwiler *et al*. [34] demonstrated a cantilevered piezoelectric composite plate with a continuous electrode layer, in which the induced electric potential is an average value. The electric potential is dependent on the integrated strain rates over the electrode area, which is known as the integrated effect of the piezoelectric sensor [35]. The designed electrodes of the Cu foil and Al film are continuous electrodes on both sides of the piezoelectric ZnO layer. The electric potential is an average value. Equation (2.15) must therefore be corrected by using the half-maximum axial strain on the ZnO layer. The integrated effect is also applied in establishing the boundary condition of the piezoelectric cantilevered ZnO layer in the simulation process.

$$V' = \frac{3\eta_1 E_{\mathrm{PET}} z_{\mathrm{ZnO}} U_z(l) t_{\mathrm{ZnO}} d_{31}}{2l^2 \varepsilon_{33}} \tag{2.16}$$

The axial stress is applied repeatedly with a resonant frequency of ω_n (Hz), and the maximum electric power of the ZnO layer is obtained without any resistive load [36]:

$$P = V' Q \omega = \frac{9\eta_1^2 E_{\mathrm{PET}}^2 z_{\mathrm{ZnO}}^2 U_z^2(l) t_{\mathrm{ZnO}} w d_{31}^2 \omega_n}{2l^3 \varepsilon_{33}} \tag{2.17}$$

2.2.5 Vibration-Induced Electric Potential and Electric Power

In this study, a sinusoidal signal $y(t) = u_0 \cos(\omega\ t)$ excitation was applied persistently at the anchor of the cantilever. The deflection $U_z(x,t)$ was assumed, and the Euler–Bernoulli beam model was adopted for simulation. The continuous system dynamic behavior can be modeled:

$$\frac{\partial^2}{\partial x^2}\left[EI\frac{\partial^2 U_z(x,t)}{\partial x^2}\right] + m\frac{\partial^2 U_z(x,t)}{\partial t^2} + b_{\mathrm{m}}\frac{\partial U_z(x,t)}{\partial t} = F_z(x,t) = -mu_0\omega^2\cos(\omega t) \tag{2.18}$$

where EI is the flexural stiffness of the plate, $U_z(x,t)$ denotes the vertical deflection of the mass point, m is the mass per unit length of the plate, b_{m} is the damping per unit length, $F_z(x,t)$ is the force per unit length, and u_0 is the amplitude of shaker vibration.

The maximum vertical deflection in the free end of the cantilever, when the excited frequency is equal to the resonant frequency (i.e. $\omega = \omega_n$), is defined [37]:

$$U_z(l,\omega_n) = \frac{A_n(l) m u_0}{\xi} \frac{[\cos(k_n l)\sinh(k_n l) - \cosh(k_n l)\sin(k_n l)]}{\sin(k_n l) + \sinh(k_n l)} \tag{2.19}$$

where ξ is the damping ratio of the cantilevered structure, defined

$$\xi = b_m / c_c = b_m / 2\sqrt{km} \tag{2.20}$$

where c_c is the critical damping coefficient, k is the equivalent spring constant ($k = 3E_{PET}I/l^3$), $m = lw(\rho_{PET}t_{PET} + \rho_{ZnO}t_{ZnO} + \rho_{Cu}t_{Cu})$ denotes the mass of the composite plate [38], and A_n is an integration constant.

By combining Equations (2.16), (2.17), and (2.19), the maximum electric potential ($\overline{V}$) and maximum electric power ($\overline{P}$) in the resonant state are defined:

$$V = \frac{3\eta_1 E_{PET} z_{ZnO} t_{ZnO} d_{31} A_n(l) m u_0}{2l^2 \varepsilon_{33} \xi} \frac{[\cos(k_n l)\sinh(k_n l) - \cosh(k_n l)\sin(k_n l)]}{\sin(k_n l) + \sinh(k_n l)} \tag{2.21}$$

$$P = \frac{9\eta_1^2 E_{PET}^2 z_{ZnO}^2 t_{ZnO} w d_{31}^2 \omega A_n^2(l) m^2 u_0^2}{2l^3 \varepsilon_{33} \xi^2} \left\{ \frac{[\cos(k_n l)\sinh(k_n l) - \cosh(k_n l)\sin(k_n l)]}{\sin(k_n l) + \sinh(k_n l)} \right\}^2 \tag{2.22}$$

The analytical model shows that the harvested vibration-induced electric potential and electric power are proportional to the ratio of the elastic constant η_1, elastic constant for the PET substrate E_{PET}, the distance z_{ZnO} from the geometric center of the ZnO layer to the neutral axis, the thickness of ZnO thin film t_{ZnO}, the transverse piezoelectric strain coefficient d_{31}, the mass density of the composite plate m, and the amplitude of shaker vibration u_0. However, the harvested vibration-induced electric potential and electric power are inversely proportional to the length of the cantilevered plate l, the dielectric coefficient of ZnO thin film ε_{33}, and the damping ratio ξ.

2.2.6 *Static Analysis to Calculate the Optimal Thickness of the PET Substrate*

To calculate the optimal thickness of the PET substrate, the FEA package ANSYS is used to perform static analysis, the results of which are compared to those obtained using Equation (2.1). The composite cantilever plate is then loaded with a constant deflection ($U_z = -2$ mm) as shown in Figure 2.6a and the optimal thickness of the PET substrate is corrected gradually. In the simulation process, a square composite structure with an effective area of 0.01×0.01 m^2 is constructed using different thicknesses of the PET substrate. The variation of the substrate thickness and the electric potential of the ZnO layer are shown in Figure 2.7. The optimal thickness of the PET substrate cannot be around 212–213 μm. Figure 2.7 shows that the resonant frequency is a function of the thickness of the PET substrate according to model analysis, as the resonant frequency depends on the substrate stiffness. Three points in the anchor of the cantilever plate are selected to analyze the internal stress and strain on the x-axis, as shown in Figure 2.6b. The thickness of the PET substrate is gradually accumulated with the internal strain on the x-axis, as shown in Figure 2.8. Point 1 indicates a long

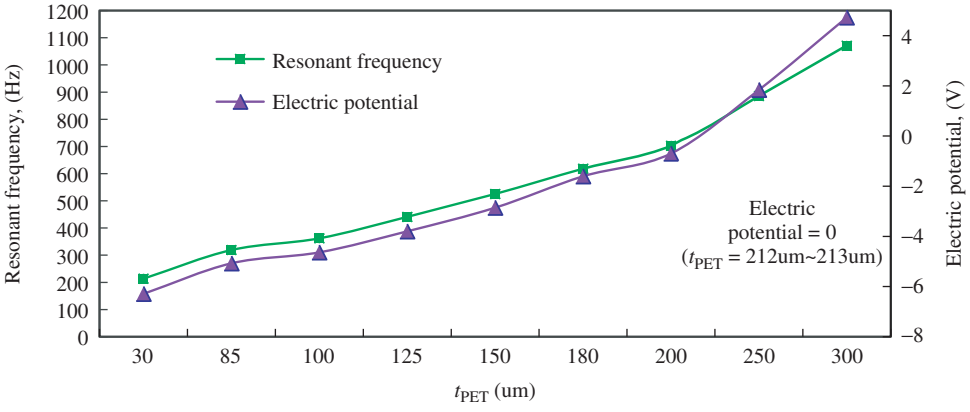

Figure 2.7 Variation of the accumulated thickness of PET substrate with the electric potential of ZnO layer and resonant frequency [29]

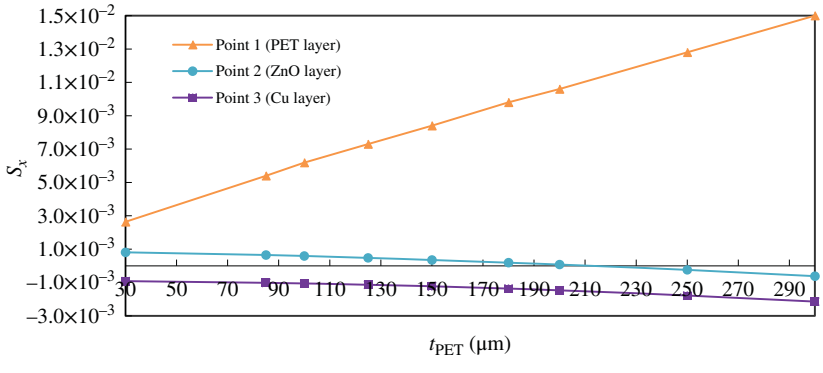

Figure 2.8 Variation of the accumulated thickness of PET substrate with the internal strain in the x-axis [29]

distance from the neutral axis to the top of the PET substrate, compared to the other two points. Therefore, the top of the PET layer receives a maximum tensile strain. The different thicknesses of the PET substrate with the internal stress in the *x*-axis are shown in Figure 2.9. There is a noticeable trend in the *x*-axis stress distribution of the three layers. The internal stress of the ZnO layer and Cu foil layer are enhanced because of the ratio of the elastic constants η_1 and η_2. The internal stress distribution of the ZnO layer and Cu foil layer is therefore obvious compared to that of the PET layer.

The simulation result shows that the neutral axis is within $\overline{Z} = 10-20$ μm when the thickness of the PET substrate is 30 μm. The neutral axis is within $\overline{Z} = 32-57$ μm when the thickness of the PET substrate is 300 μm. When the thickness of the PET substrate

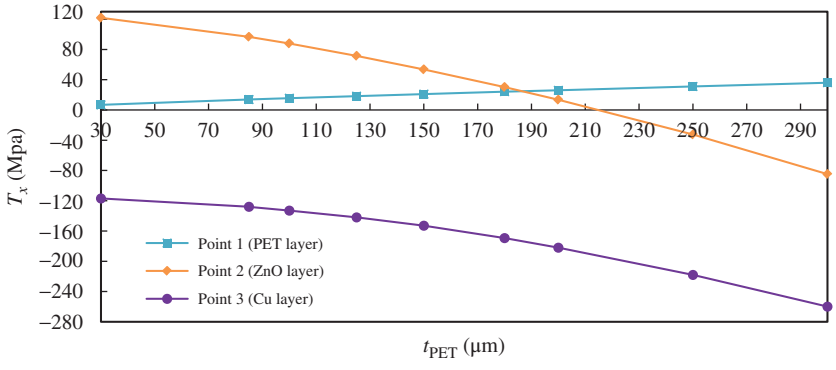

Figure 2.9 Variation of the accumulated thickness of PET substrate with the internal stress in the x-axis [29]

is smaller than 212.5 μm, the tensile strain and stress are within the piezoelectric ZnO layer. The compressive strain and stress are within the piezoelectric ZnO layer when the thickness is greater than 212.5 μm; consequently, a positive electric potential is induced. If we select a material that is of a higher elastic constant than the PET, the elastic constant ratio η_1 of the substrate would be lower. Thus, the x-axis stress and the induced electric potential on the ZnO layer would be reduced, as seen from Equations (2.10) and (2.15). In addition, a thicker and stiffer substrate creates a lower vertical tip deflection and a lower electric potential. A thin substrate with stiffness that is too weak to counteract the input vibrational energy increases the mechanical damping ratio, as described by Equation (2.20). The optimal thickness of the PET substrate is therefore 100 μm.

2.2.7 Model Analysis and Harmonic Analysis

A square structure with an effective area of $0.01 \times 0.01\ m^2$ was developed during the simulation process. Modal analysis and harmonic response analysis were performed to obtain the structural modal parameters, frequency response functions, and the induced voltage from the ZnO layer.

The layout of the flexible piezoelectric harvester is shown in Figure 2.10, depicting the schematic piezoelectric composite plate and the designed dimensions. Table 2.2 lists the design parameters of these five harvesters, the lengths of the lump structure W_1 and W_2, the gaps L_1 and L_2 between W_1 and W_2, and the thickness of the lump structures p.

Three-dimensional (3D) FEMs of the flexible piezoelectric cantilever plate were constructed using a Solid5 3D-coupled field element. The FEMs are shown in Figure 2.11. The physical properties of the materials and the piezoelectric matrix of

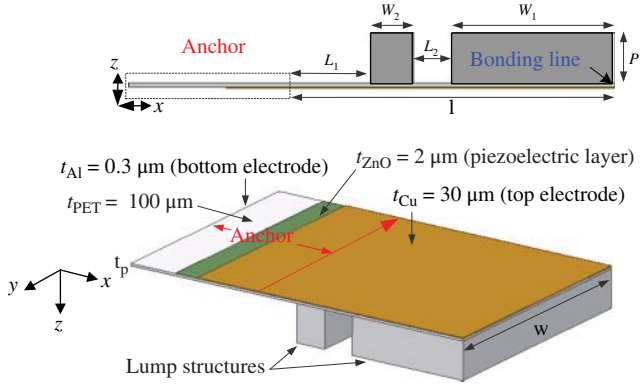

Figure 2.10 Schematic layout of flexible piezoelectric harvester and designed parameters [29]

Table 2.2 Properties of five harvesters [28]

Case No.	Length of lump structure W_1 (m)	Length of lump structure W_2 (m)	Gap between W_1 and W_2 (m)	Thickness of lump structure p (μm)
1	0.005	0	$L_1 = 0.005$ $L_2 = 0$	2000
2	0.005	0.0025	$L_1 = 0.00125$ $L_2 = 0.00125$	1600
3	0.0025	0.0025	$L_1 = 0.0025$ $L_2 = 0.0025$	400
4	0	0.0025	$L_1 = 0.005$ $L_2 = 0.0025$	400
5 (no lump)	–	–	–	–

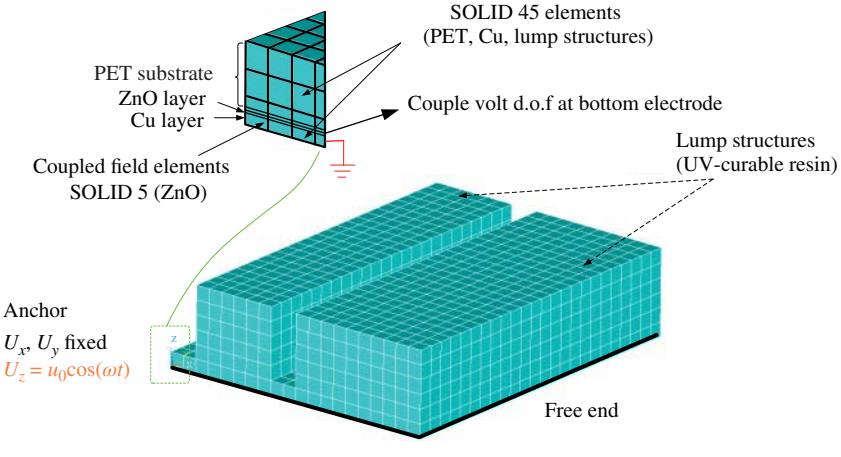

Figure 2.11 Plot of the finite element mesh model of Case 2

Table 2.3 Physical properties of the four materials [28]

Material properties	PET substrate	ZnO	Cu electrode	Exposed UV-curable resin
Young's modulus E (N m^{-2})	2.4×10^{9}	$[c]_{6\times6}$ (see Table 2.4)	1.19×10^{11}	2.4×10^{9}
Density ρ (kg m^{-3})	1400	5665	8900	1037.78
Poisson ratio υ	0.36	–	0.326	0.34

ZnO thin film are listed in Tables 2.3 and 2.4. Modal analysis is performed to obtain the structural modal parameters. Furthermore, for the harmonic response analysis process, $y(t) = u_0 \cos(\omega\, t)$ sinusoidal signals were applied on the anchor side of the cantilever plate. The amplitude of the vibration was set at a fixed displacement.

2.2.8 Results of Model Analysis and Harmonic Analysis

The result shows that the first mode of Case 2 (Table 2.2) is the uniform bending mode. Therefore, the maximum electric potential of Case 2 can also be obtained in the first mode. The first two resonant frequency mode shapes of Case 2 are shown in Figure 2.12; the first resonant frequency $\omega_n(1)$ was 225.173 Hz. In the second mode however (resonant frequency at 1593 Hz), an inflection point occurred in the middle of the composite cantilever plate which eliminated the induced voltage on the ZnO layer because of the charge cancellation. The vibration amplitude and displacement response when the cantilever plate operated at resonance frequency are shown in Figure 2.13. The induced maximum upward and downward deflection was observed when the vibration amplitude shifted to origin (Figure 2.13).

Figure 2.14 shows the resonant frequency mode shapes of five cases, which could be obtained at 151.432, 225.173, 315.605, 401.145, and 356.744 Hz. Table 2.5 lists the resonant frequencies, tip deflection, damping ratio, and electric potential of the five cases. The results show that the damping ratio of Cases 1 and 2 is smaller than that of the other three cases. The vertical deflection and maximum electric potential have the same trend. The stiffness of the five cases is the same because they were all designed using the same composite substrate (l, w, t_{PET}, t_{ZnO}, and t_{Cu} are constant). The selectively deposited UV-curable resin lump structures used as an additional mass were added to the cantilever plate to change the resonant frequency, reduce the damping ratio, and achieve a large tip deflection of a single harvester, as expressed in Equations (2.19) and (2.20). Figure 2.15a shows that Case 1 has the maximum deflection of 2123.3 μm; Case 2 has 1456.2 μm, Case 3 has 769.4 μm, Case 4 has 454.4 μm, and Case 5 has 404.4 μm. Figure 2.15b shows that Case 1 has the maximum electric potential of 3.998 V; Case 2 has 2.521 V, Case 3 has 1.47 V, Case 4 has 0.858 V, and Case 5 has 0.697 V (Table 2.2).

Table 2.4 Material properties matrix of piezoelectric ZnO thin film [28]

ZnO stiffness matrix $[c]$ ($\mathrm{N\,m^{-2}}$)

$$[c] = \begin{bmatrix} 20.97 & 12.11 & 10.51 & 0 & 0 & 0 \\ 12.11 & 20.97 & 10.51 & 0 & 0 & 0 \\ 10.51 & 10.51 & 21.09 & 0 & 0 & 0 \\ 0 & 0 & 0 & 4.43 & 0 & 0 \\ 0 & 0 & 0 & 0 & 4.24 & 0 \\ 0 & 0 & 0 & 0 & 0 & 4.24 \end{bmatrix}_{6\times6} \times 10^{10}$$

ZnO compliance matrix $[s]$ ($\mathrm{m^2\,N^{-1}}$)

$$[s] = \begin{bmatrix} 7.85525 & -3.43143 & -2.20457 & 0 & 0 & 0 \\ -3.43143 & 7.85525 & -2.20457 & 0 & 0 & 0 \\ -2.20457 & -2.20457 & 6.93884 & 0 & 0 & 0 \\ 0 & 0 & 0 & 22.5734 & 0 & 0 \\ 0 & 0 & 0 & 0 & 23.5849 & 0 \\ 0 & 0 & 0 & 0 & 0 & 23.5849 \end{bmatrix}_{6\times6} \times 10^{-12}$$

ZnO piezoelectric stress matrix $[e]$ ($\mathrm{C\,m^{-2}}$)

$$[e] = \begin{bmatrix} 0 & 0 & -0.570878 \\ 0 & 0 & -0.570878 \\ 0 & 0 & 0.428446 \\ 0 & 0 & 0 \\ 0 & -0.480816 & 0 \\ -0.480816 & 0 & 0 \end{bmatrix}_{6\times3}$$

ZnO piezoelectric strain matrix $[d]$ ($\mathrm{C\,N^{-1}}$)

$$[d] = \begin{bmatrix} 0 & 0 & -3.47 \\ 0 & 0 & -3.47 \\ 0 & 0 & 5.49 \\ 0 & 0 & 0 \\ 0 & -11.3 & 0 \\ -11.3 & 0 & 0 \end{bmatrix}_{6\times3} \times 10^{-12}$$

ZnO dielectric matrix $[\varepsilon_r]$ under the constant strain

$$[\varepsilon_r] = \begin{bmatrix} 7.57 & 0 & 0 \\ 0 & 7.57 & 0 \\ 0 & 0 & 8.31 \end{bmatrix}_{3\times3}$$

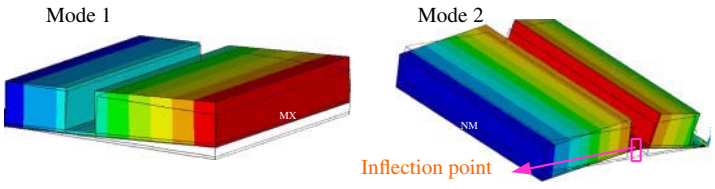

Figure 2.12 (a,b) The first and second resonance mode shapes of Case 2

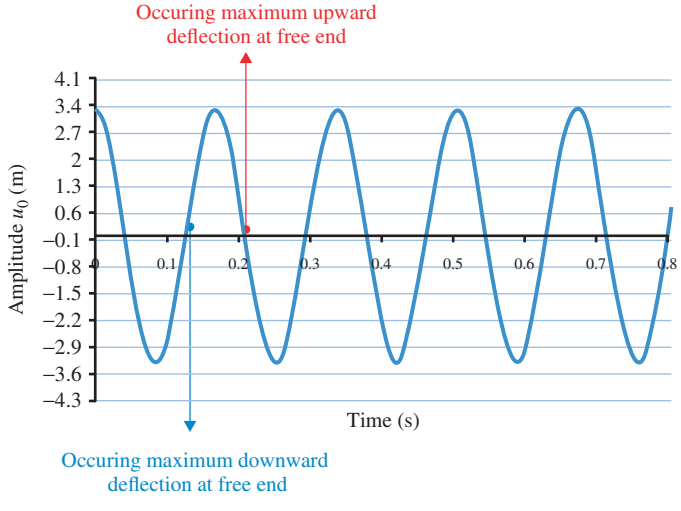

Figure 2.13 The harmonic response analysis of Case 2: vibration process (excited frequency of 225.173 Hz and a fixed sinusoidal vibration amplitude of 33 μm at the anchor side)

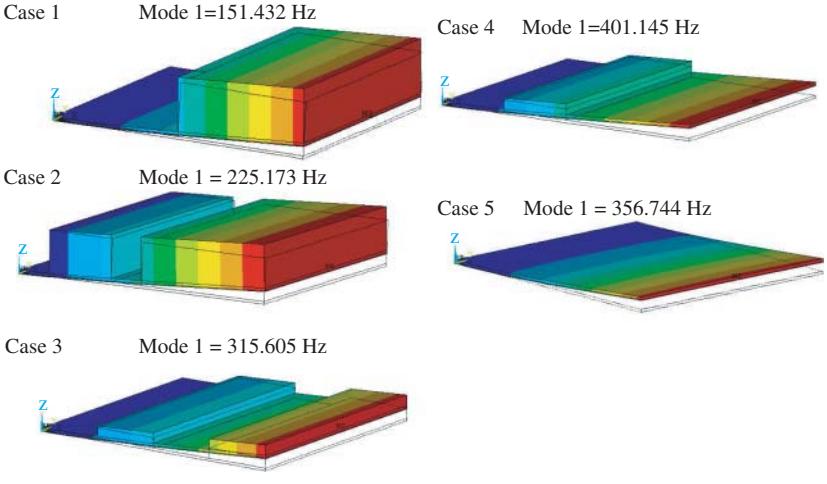

Figure 2.14 (a–e) The simulated results of the first resonance mode of five cases [29]

Table 2.5 Resonant frequencies, tip deflection, damping ratio, and electric potential for simulation [28]

Case No.	$\omega_{n(1)}$ (Hz)	Damping ratio ξ	Tip deflection U_z (μm)	Electric potential (OCV) (V)
1	151.432	0.01043	2123.3	3.990
2	225.173	0.01634	1456.2	2.523
3	315.605	0.03198	769.4	1.473
4	401.145	0.06128	454.4	0.853
5 (no lump)	356.744	0.0653	404.4	0.698

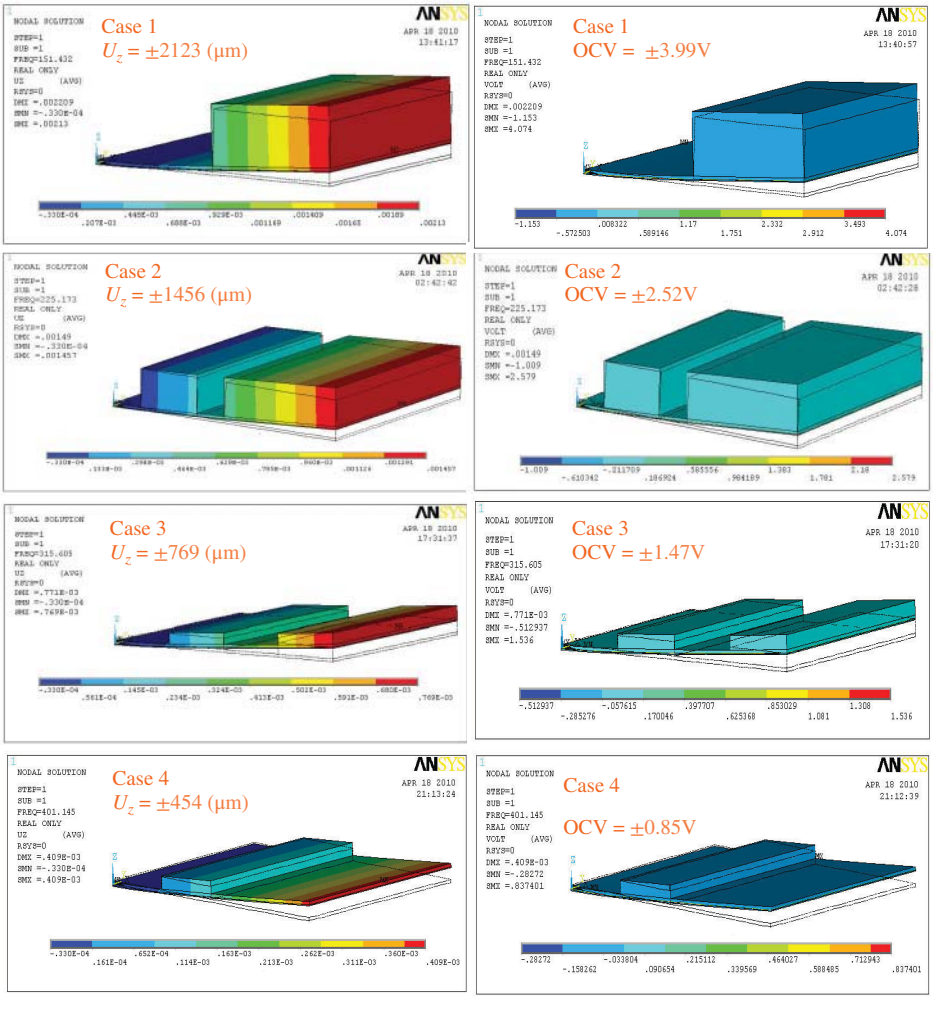

Figure 2.15 The simulated results of four cases: (a) plots of the deflection and (b) plots of the electric potential [28]

2.3 The Fabrication of Flexible Piezoelectric ZnO Harvesters on PET Substrates

2.3.1 Bonding Process to Fabricate UV-Curable Resin Lump Structures on PET Substrates

The harvester fabrication procedure using the bonding process is described in the following.

2.3.1.1 Fabrication of a PMMA Template

A micro computer numerical control (CNC) machining center is used to machine a polymethyl methacrylate (PMMA) billet into desired shapes. When the template is completed (Figures 2.16 and 2.17a), the template is sprayed with release agents.

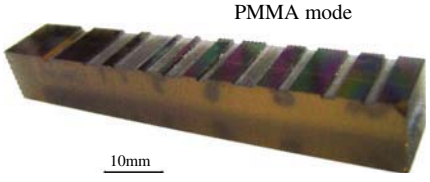

Figure 2.16 PMMA template machined by end mill

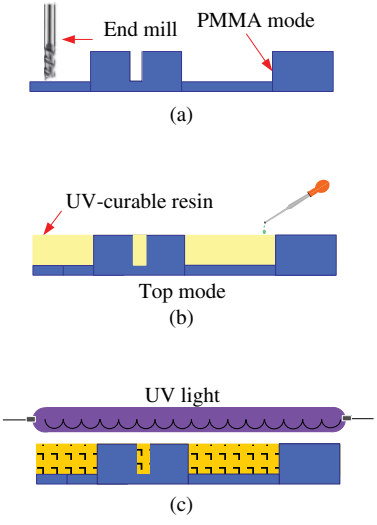

Figure 2.17 Illustration of fabrication process of top mode (a) the template is machined, (b) the UV curable resin is cast in the template, and (c) UV light exposes the resin

The UV-curable resin is injected uniformly into the cavities (Figure 2.17b). Exposure to UV light (the exposure dosage is from 350 to 450 mJ cm^{-2}) solidifies the resin (Figure 2.17c).

2.3.1.2 Definition of Bonding Pad

The PET flexible substrate is coated with a thick photoresistant SU-8 and the bonding pad region for subsequent bonding is defined, followed by an exposure process and a developmental process. It is then injected with thin UV-curable resin to complete the bonding pad for the bonding process (Figure 2.18a–c).

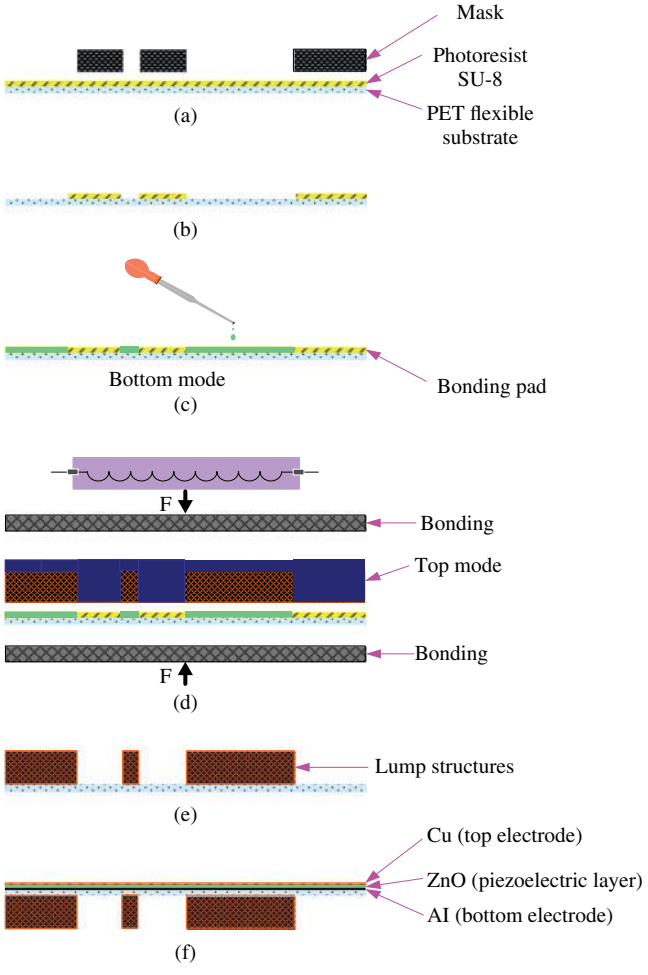

Figure 2.18 Illustration of fabrication process of lump structures on flexible multilayer plate (a) exposure process, (b) patterning on PET flexible substrate, (c) bonding process, (d) UV curing, (e) lump structures making, and (f) Cu/ZnO/Al layer with lump structures

2.3.1.3 Bonding Process

The bonding process is used to transfer the exposed UV-curable resin to the selected area on the PET flexible substrate. First, the top mode is flipped with the exposed UV-curable resin. Both the top and bottom modes are aligned and pressed. The UV light then causes the lump structures to transfer to the PET subtract accurately, and the exposure dosage is from 350 to 450 mJ cm^{-2}. Secondly, the dilute acetone is used to remove the residual photoresistant SU-8 with an ultrasonic cleaner (Branson Model 1510). Thirdly, the PET substrate with lump structures is easily separated from the template when the template is sprayed with some release agents. Finally, the PET substrate with lump structures is flipped, and the Al, ZnO, and Cu layers are continuously fabricated on the PET substrate surface (Figure 2.18d–f).

2.3.2 Near-Field Electro-Spinning with Stereolithography Technique to Directly Write 3D UV-Curable Resin Patterns on PET Substrates

To fabricate the selectively deposited UV-curable resin lump structures as a proof mass, electrospinning [30] and stereolithography [31] techniques were used to directly draw patterns on the back of the PET-based piezoelectric composite substrate, as shown in Figure 2.19a. This lithography-free method can improve the imprinting process, and can be applied to transfer UV-curable resin configurations onto a PET substrate. Electrospinning equipment in tandem with a UV light source (Hamamatsu co. LCS LightningCure^{TM}), high-voltage power supply (HP 6515A), X-Y stage (Tanlian electro optics co. TL-ST9090-50), and infusion pump (KDS 101) were assembled, as shown in Figure 2.19b. The UV-curable resin was selectively spun on the PET flexible substrate by using a high electric field ($5 \times 10^6 - 1.6 \times 10^7$ V m^{-1}) and controllable infusion pump (1 mL min^{-1}). Subsequently, the UV light exposed the patterns to immediately solidify the resin (exposure dosage at 400 mJ cm^{-2}), based on layer-by-layer processing.

2.3.3 Sputtering of Al and ITO Conductive Thin Films on PET Substrates

The conductive Al and ITO films were deposited directly onto the PET substrate by using RF magnetron sputtering at room temperature (Al/PET and ITO/PET) and subsequent ZnO deposition (ZnO/Al/PET and ZnO/ITO/PET). The fabrication procedures include PET substrate cleaning followed by sputtering Al and ITO as conductive substrates.

The PET substrates were cleaned ultrasonically in toluene, isopropyl alcohol, and methanol for 10 minutes each. The pre-deposited PET substrate surfaces were then cleaned using plasma in a vacuum.

After cleaning the PET substrates, an Al thin film (200 nm) was selected as the conductive electrode by using sputtering deposition; its low sheet resistance and matching

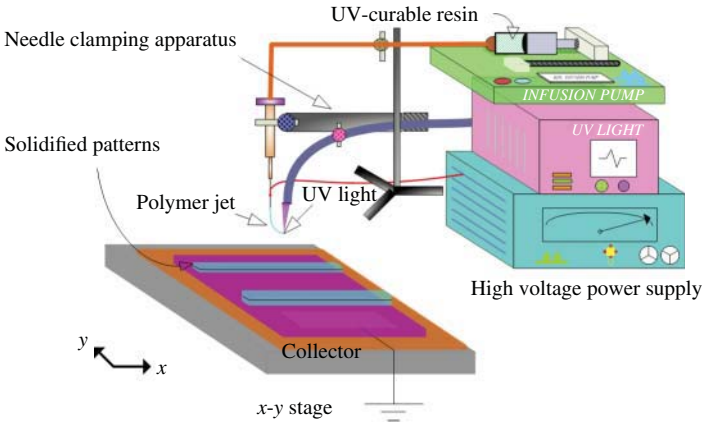

(a)

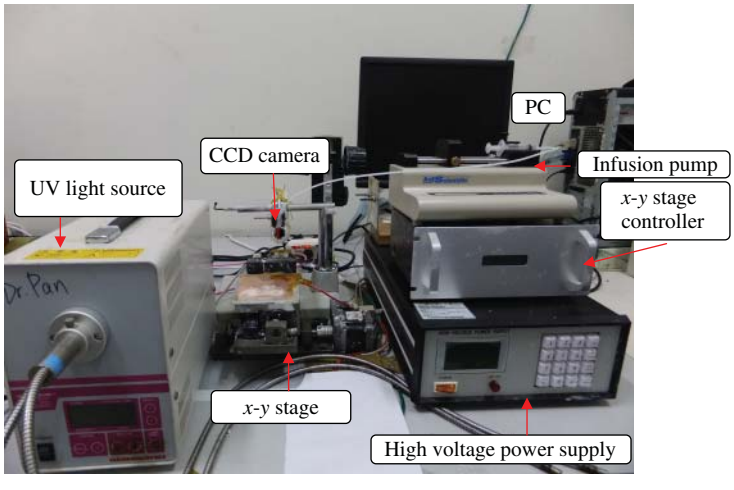

(b)

Figure 2.19 Fabrication processes of electrospinning with stereolithography technique based on UV-curable resin to fabricate 3D patterns on PET substrate: (a) schematic diagram of equipment and (b) experimental apparatuses

lattice constants with ZnO thin film provide favorable adhesion. The Al film sheet resistance was below 9.7 Ω/sq (ohms per square). The process parameters are shown in Table 2.6. Conversely, ITO film (200 nm) was also deposited onto the PET substrate as the conductive electrode. ITO films were deposited using RF reactive magnetron sputtering [32]. The sheet resistance of the ITO films was below 117.5 Ω/sq. Table 2.7 lists the process parameters.

Table 2.6 Al sputtering deposition parameters [28]

Target	Substrate temperature	Ar flow rate (sccm)	Sputtering pressure (mTorr)	DC power (W)
Al (99.9%)	RT	7.6	3	300

Table 2.7 ITO sputtering deposition parameters [28]

Alloy target	Substrate temperature (°C)	Ar flow rate (sccm)	Sputtering pressure (mTorr)	RF power (W)
In_2O_3:SnO_3 (90:10) (99.9%)	30	6.5	15	30

Table 2.8 Sputtering parameters of ZnO thin film [28]

Target	Substrate temperature	$O_2/Ar + O_2$ (%)	Sputtering pressure (mTorr)	RF power (W)
Zn (99.995%)	RT	60	12	75

2.3.4 Deposition of Piezoelectric ZnO Thin Films by Using RF Magnetron Sputtering

An RF reactive magnetron sputtering method was employed to deposit ZnO piezoelectric thin films. A metallic zinc disk with a 5 cm (2 inches) diameter and a thickness of 0.6 cm (0.25 inch) with 99.995% purity was used as the target. After the base pressure was evacuated below 6×10^{-6} Torr, O_2 and Ar gases were introduced into the chamber as a gas atmosphere during sputtering. The shutter was opened to start sputtering for 1 hour after 30 minutes of pre-sputtering. Table 2.8 lists the optimal sputtering parameters of work pressure, RF power, and O_2 concentration. The ZnO thin film of 2 μm was then deposited on the Al/PET and ITO/PET at room temperature.

For energy harvester applications, the physical properties of piezoelectric ZnO thin films should theoretically have precise surface structures and high *c*-axis orientations. The flexible multilayer structures (Al/PET, ITO/PET, ZnO/ITO/PET, and ZnO/Al/PET) are shown in Figure 2.20a. The surface morphologies of the deposited thin films were investigated. The SEM images of films are shown in Figure 2.20b–e. The crystallite size of Al films deposited on the PET substrate (Figure 2.20b) is uniform and clear compared with the ITO film on the PET substrate (Figure 2.20c).

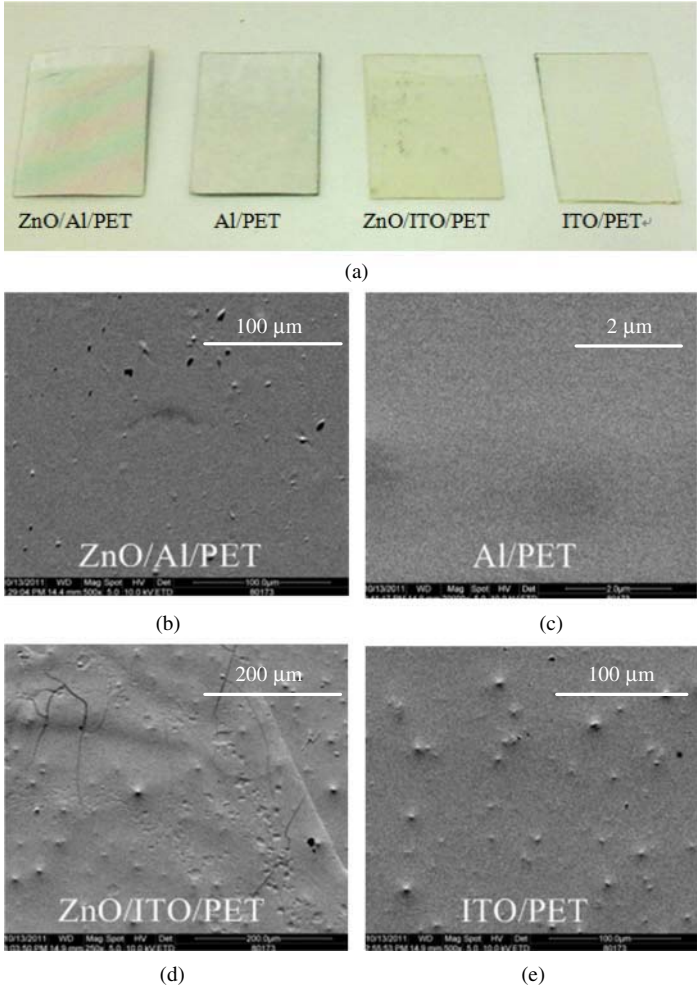

Figure 2.20 Flexible multilayer plate prototypes and images of the coating layer surfaces deposited on PET substrate: (a) four prototypes, (b) ZnO/Al/PET, (c) Al/PET, (d) ZnO/ITO/PET, and (e) ITO/PET

Furthermore, when the ZnO thin film was deposited on the Al/PET conductive substrate (Figure 2.20d), the crystallite structure was composed of many circle-like grains [33, 34] as shown in Figure 2.21a. The uniform grain size distribution was homogeneous with a smooth surface compared with the ZnO thin film deposited on the ITO/PET conductive substrate because the ITO film surface is relatively rough (Figure 2.20e). The microstructure and thickness of various films were evaluated, and the cross-sectional SEM images of ZnO/Al/PET composite structures are shown in Figure 2.21b.

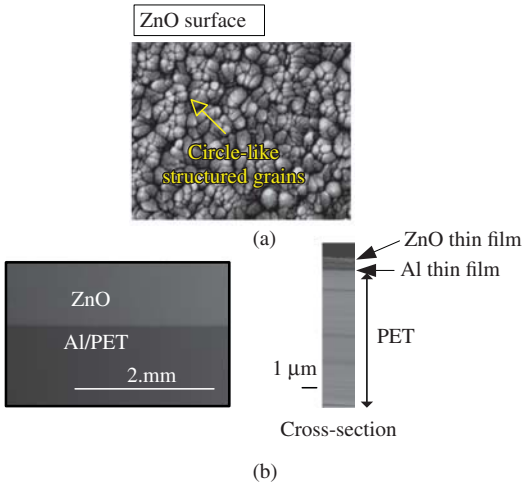

Figure 2.21 (a) SEM observations of the surface morphology of ZnO thin film on Al/PET substrate and (b) the cross-sectional SEM image of ZnO/Al/PET composite structures

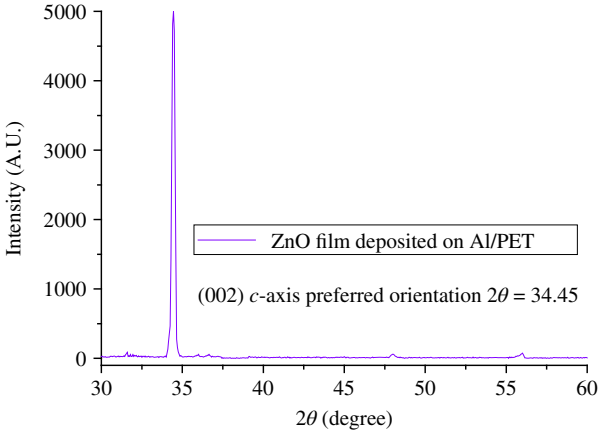

Figure 2.22 XRD patterns of ZnO thin film deposited on Al/PET (ZnO thin film was developed at room temperature with RF power of 75 W, a mixed gas $O_2/Ar + O_2$ of 60%, sputtering pressures of 15 m Torr, and base pressure of 6×10^{-6} Torr) [29]

The preferred orientation and crystal properties of the ZnO thin films were evaluated using XRD (X-ray diffraction) (a Shimadzu XRD-6000 with CuKα radiation). Figure 2.22 shows a high (002) diffraction peak at $2\theta = 34.45°$ of the ZnO thin film. The precise circle-like grains with such orientation of ZnO thin film exhibit excellent piezoelectricity.

The effects of RF magnetron sputtering parameters on the luminescent characteristics of ZnO thin films were also investigated. The optimal sputtering parameters for

the most favorable photoluminescence (PL) characteristics were determined. In the PL spectrum, only UV light of 379 nm wavelength (UV region) appeared, and no visible light could be detected. The photon energy of the characteristic UV light is 3.27 eV, which corresponds to the band gap of ZnO as shown in Figure 2.23. The luminescence mechanisms of UV and visible light emissions of ZnO thin films were considered in the case of band-to-band transition and existing defects involved in ZnO. From the results of XRD and PL analyses the sputtering-deposited ZnO thin film exhibits excellent piezoelectric properties, demonstrating that it is suitable for use as a piezoelectric material for generators.

Figure 2.24a shows the prototype of the four flexible energy harvesters. It reveals that a commercial PET substrate of $t_{PET} = 100\,\mu m$ can reduce the warping effect and obtain a uniform cantilever plate. By contrast, a thin PET substrate of approximately $t_{PET} = 30–80\,\mu m$ in thickness causes a severe warping effect because of thermal deformation during the sputtering process, as shown in Figure 2.24b. Selecting a suitable thickness of the PET substrate provides more robustness in controlling the warping deformation.

2.3.5 *Testing a Single Energy Harvester under Resonant and Non-Resonant Conditions*

The harvester was placed on a vibration platform of a shaker (B&K BK4800) at an adjustable vibration frequency. To supply suitable acceleration to the harvester, the amplitude of vibration was set at a fixed displacement ($u_0 = 33\,\mu m$). The shaker can

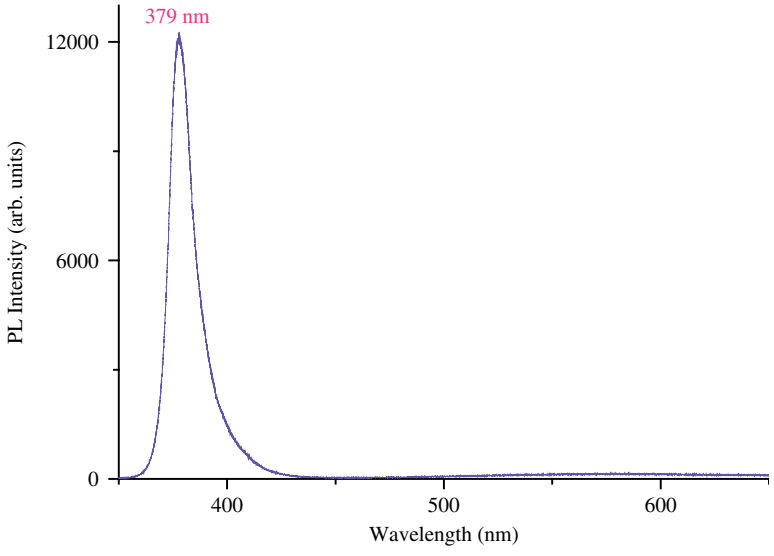

Figure 2.23 The PL spectra of ZnO thin film with optimal sputtering parameters

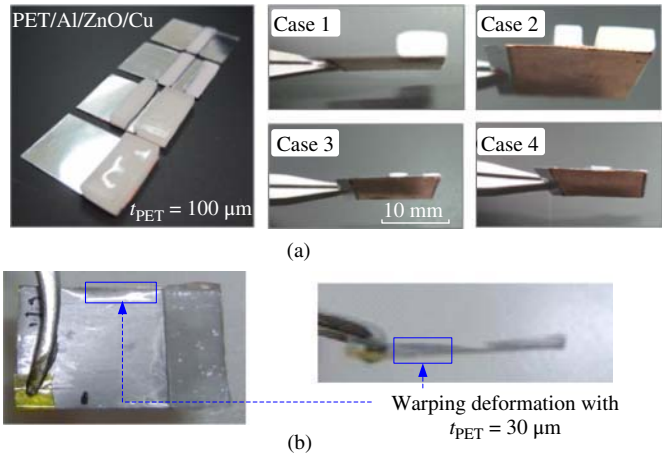

Figure 2.24 Prototype of energy harvesters: (a) the four energy harvesters with PET thickness of 100 μm and (b) a severely warping cantilever plate with $t_p = 30$ μm [29]

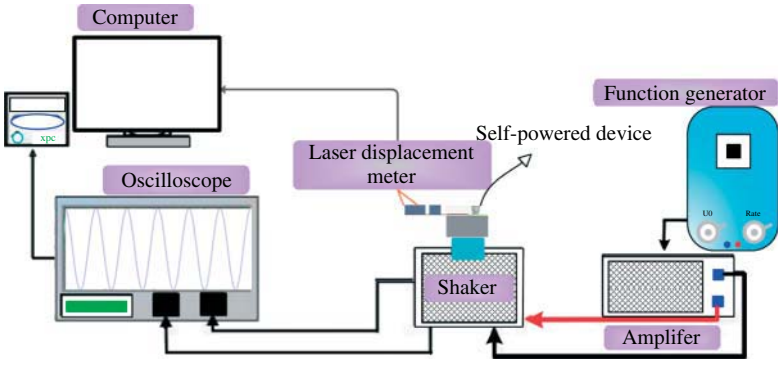

Figure 2.25 The measurement system for the self-powered flash signal LED module

be controlled by the function generator. The induced voltage signal from the harvester was measured using an oscilloscope (Agilent 54622D). A laser displacement meter (Keyence LK-G5001V) can be used to measure the vertical deflection at the free end of the cantilever plate. The measurement system is schematically shown in Figure 2.25. Figure 2.26 shows the energy-harvesting system, which consists of the rectifying bridge and a storage electrolytic capacitor.

Case 2 (Table 2.2) was directly excited at a fixed amplitude of the vibration source and scanned using the frequency 200–250 Hz. Case 5 was scanned from 340 to 370 Hz. The cantilever tip deflection was measured using a laser displacement meter. The vibration amplitude at the anchor side was measured as shown in Figure 2.27a. The resonant frequency and OCV (output circuit voltage) signal were recorded using

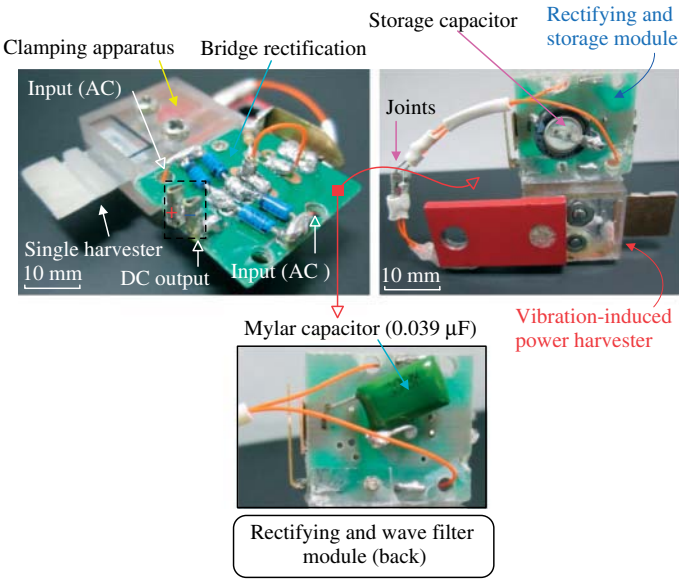

Figure 2.26 The energy harvesting system consisting of a bridge rectifier and storage capacitor or wave filter module [29]

an oscillograph. The 218 Hz mode of Case 2 is the uniform bending mode, which exhibited the largest tip deflection and maximum OCV of 2.5 V (Figure 2.27b). The OCV of Case 5 shown in Figure 2.27d was 0.6 V. Table 2.9 tabulates the experimental results of OCV, CCV (closed circuit voltage), tip deflection, DC voltage across a capacitor, and peak power for experiment. In Figure 2.26, the bridge rectifier circuit consists of four ST (SGS) 1N5711 Schottky diodes that had a lower forward voltage drop of approximately 0.2 V each; hence, the bridge rectifier circuit consumes an electric potential of approximately 0.4 V. A 0.039 μF storage capacitor was selected as the wave filter because it charges faster than storage electrolytic capacitors do. As shown in Figure 2.27c, the DC voltage of Case 2 was 2 V across a Mylar capacitor after rectification, whereas the DC voltage was 0.14 V for Case 5, as shown in Figure 2.27e.

To measure the power output, the load resistance was connected in parallel to convert the mechanical vibration to the AC load voltage. Subsequently, Case 2 was connected to an external resistance load between the two electrodes. The CCV was measured at the first mode resonance as a function of load resistance. According to the current–voltage (I–V) test, the internal resistance of various ZnO thicknesses was within 2–5 MΩ [39]. The external load must be adjusted to match the output voltage; the matching of the external load and the optimal power density was achieved by fabricating ZnO-based harvesters with a ZnO thin film thickness of 2 μm. The measurement results show that the load voltage increased with the load resistance; Case 2 reached 2.16 V, and Case 5 reached 0.24 V (Figure 2.28). In addition, Figure 2.29 shows the maximum power output of 0.556 μW from input vibrations of 61.8 m s^{-2} at 218 Hz for

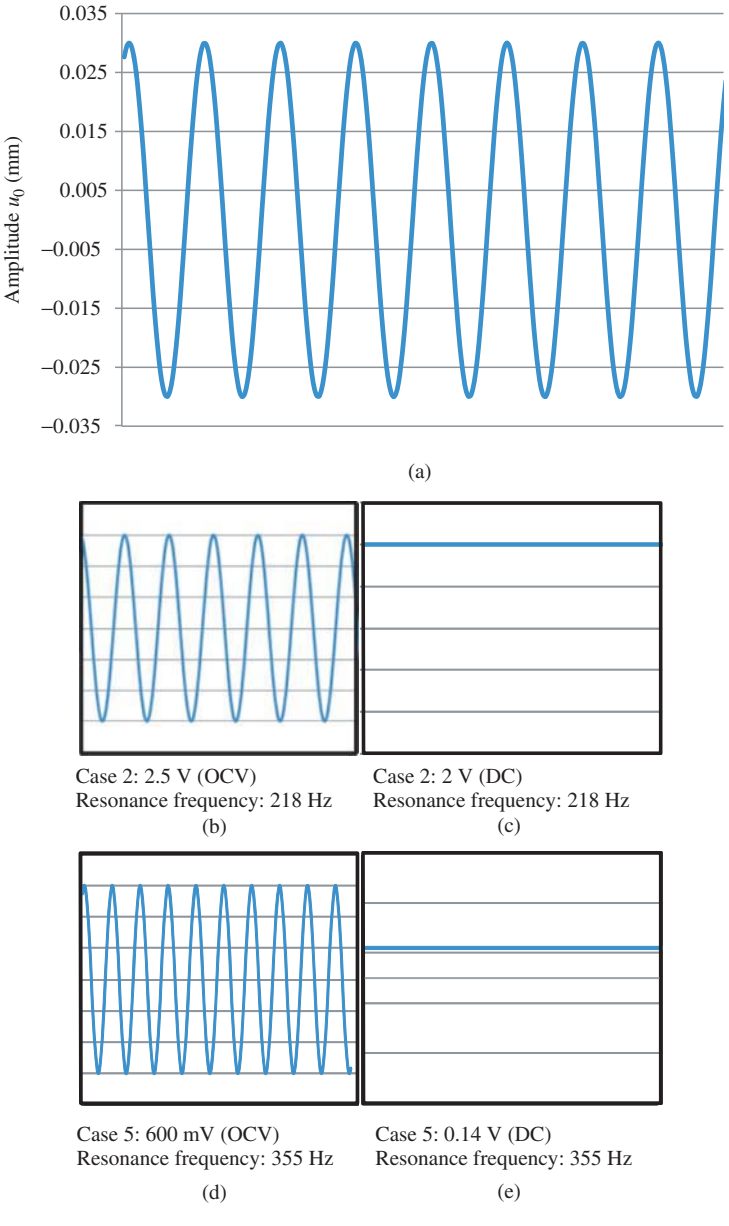

Figure 2.27 Experimental results: (a) vibration amplitude at the anchor side, (b) resonant frequency and harvested OCV signal of Case 2 (2.5 V under 218 Hz), (c) DC voltage 2 V across a 0.039 μF Mylar capacitor under 218 Hz of Case 2, (d) Case 5 (OCV 0.6 V under 355 Hz), and (e) DC voltage 0.14 V under 355 Hz of Case 5

Table 2.9 Peak voltages, tip deflection, and peak power for experiment [28]

Case No.	$\omega_{n(1)}$ (Hz)	U_z (μm)	U_z/u_0	OCV (V)	CCV (V)	Peak power (μW)	DC voltage across a capacitor (V)
Case 2	218	1456.2	44.127	2.5	2.16	0.556	2
Case 5	355	404.4	12.25	0.6	0.24	0.005	0.14

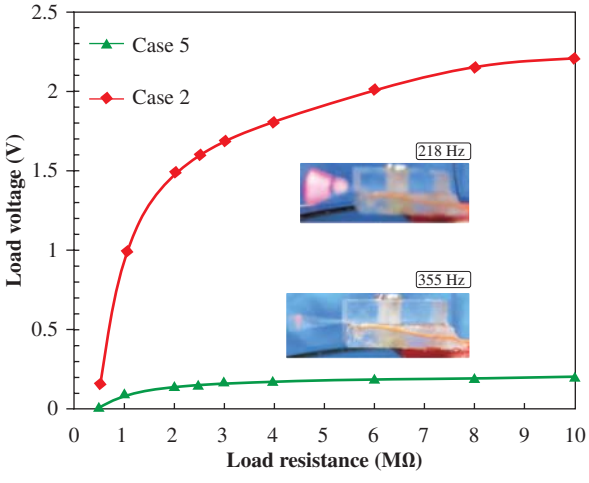

Figure 2.28 Load voltage vs. load resistance at the first mode resonance [28]

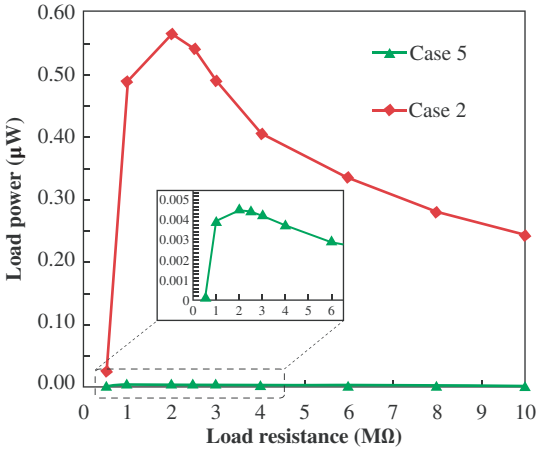

Figure 2.29 Load power vs. load resistance at the first mode resonance [28]

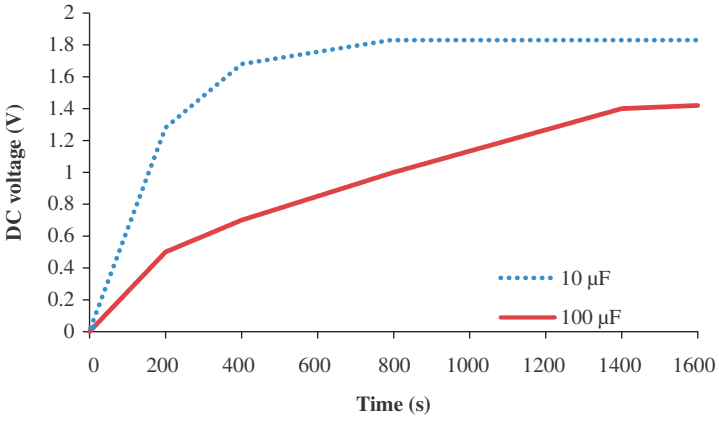

Figure 2.30 Charging results of Case 2 using 100 and 10 μF storage capacitors at 218 Hz

Case 2. Case 5 produced 0.005 μW from input vibrations of 164 m s^{-2} at 355 Hz. The output electric power was calculated according to peak power = $(CCV_{peak}/1.414)^2/R$ where R is resistance.

2.3.6 Application of ZnO/PET-Based Generator to Flash Signal LED Module

The experimental results of using this energy-harvesting system show that the charge performance of the storage capacitor is proportional to the peak power. The energy-harvesting system of Case 2 was tested at 218 Hz. The charging results of Case 2 (Table 2.2) are shown in Figure 2.30. The DC voltages across the storage capacitors (100 and 10 μF) after rectification were measured. The 100 μF storage capacitor required 2250 seconds to accumulate sufficient electrical energy of approximately 1.572 V to drive an external flash LED (light-emitting diode) module, as shown in Figure 2.31a, and the 10 μF storage capacitor required 330 seconds to store electrical energy (nearly 1.58 V).

In addition, the harvesting system was also driven using a domestic electric fan to scavenge wind power under non-resonant conditions. Figure 2.31b shows the experimental process of air flow affecting the energy harvesters. In an air flow (wind speed of 2.5 m s^{-1} and air flow of 0.56 m^3 s^{-1}), the energy harvesters regularly shed alternating vortices on either side because of the turbulence effect. The resulting pressure differential caused by the vortices forces the energy harvesters to move in an oscillating motion (a vibration frequency of 56 Hz and a tip deflection of 2125 μm were measured using a laser displacement meter). Following AC to DC rectification, the maximum DC output voltage across a 0.039 μF capacitor remained at 3.7 V. The maximum power of 1.247 μW was obtained with a load resistance of 2 MΩ. When the harvesting

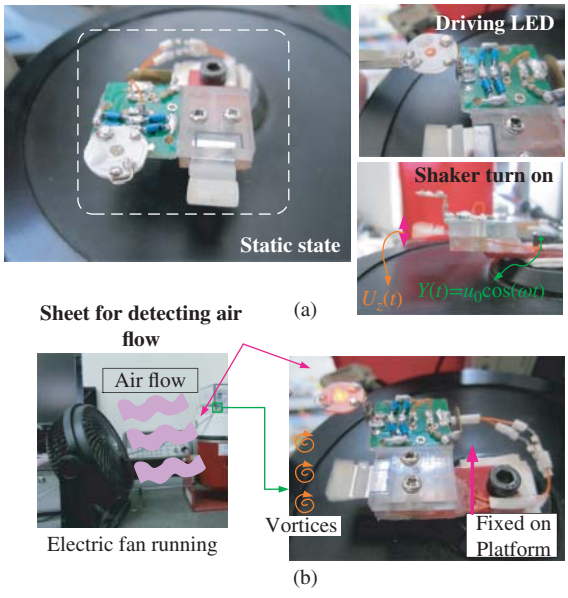

Figure 2.31 Vibration energy scavenging for self-powered flash signal LED module: (a) excited at 218 Hz by shaker and (b) excited at 56 Hz with tip deflection of 2125 μm using a domestic electric fan (wind speed: 150 m/min and air flow: 34 m^3/min)

system was running, the storage module (using a 10 μF capacitor) quickly accumulated sufficient electric potential after approximately 47 seconds and overcame the forward voltage of the LED module. Subsequently, the LED module was lit four times for a period of 2 s by the limited electrical energy output from a storage capacitor.

2.3.7 Design and Performance of a Broad Bandwidth Energy Harvesting System

Four single harvesters are assembled as an array in parallel cantilever structures, as shown in Figure 2.32. The homemade clamping apparatus is used to hold the four single harvesters. The broad bandwidth harvesting system was placed on a shaker with an adjustable vibration frequency. The shaker was controlled by the function generator with a power amplifier, and the amplitude of vibration was set at a fixed displacement to supply sufficient acceleration for the harvesting system. A laser displacement meter was used to measure the deflection in the free end of the cantilever plate. The induced electric potential signal from the harvester was measured using the oscilloscope (Figure 2.33).

To measure the resonant frequency, OCV, CCV, and load electric power, the vibration-induced energy-harvesting module with a bridge rectifier and a wave filter was prepared. To investigate the resonant mode and induced electric potential,

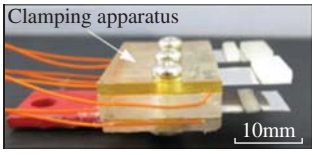

Figure 2.32 The four single harvesters are assembled as an array with a homemade clamping apparatus [29]

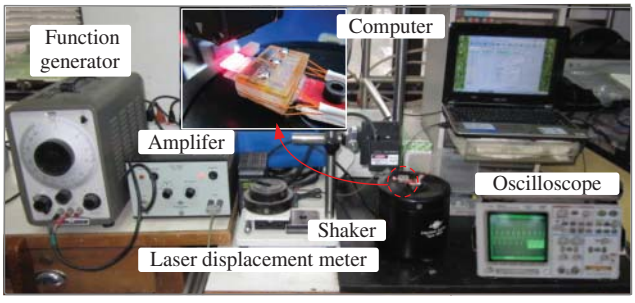

Figure 2.33 The photo of the measurement apparatuses [29]

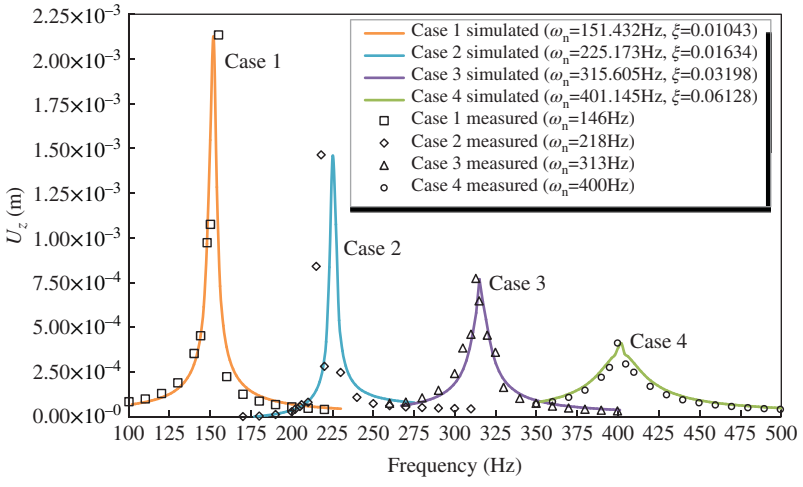

Figure 2.34 Deflection as a function of excited frequency of four cases [29]

Case 1 (Table 2.2) was directly excited at a fixed amplitude scanning of 100–230 Hz. Case 2, Case 3, and Case 4 were scanned from 175 to 315 Hz, 260 to 400 Hz, and 350 to 500 Hz, respectively. The tip deflections of the four cases are displayed in Figure 2.34, showing the simulated and experimental results. The resonant frequency of Case 1 is the minimum among the four cases, and Case 4 is the maximum case.

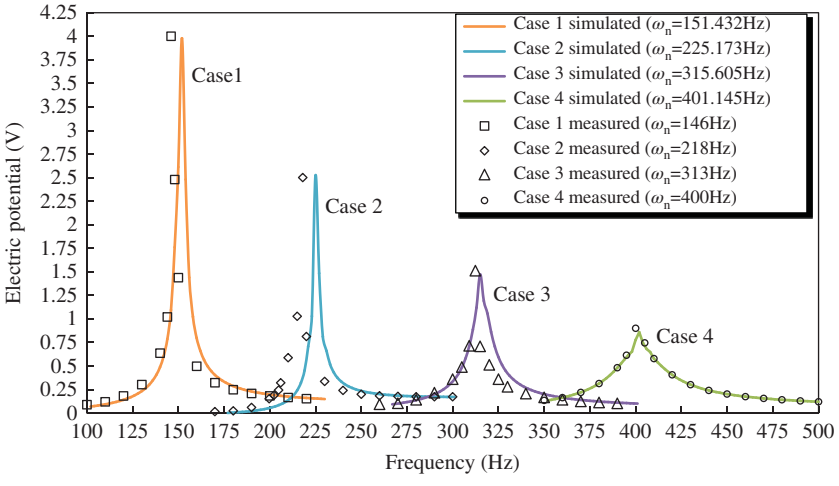

Figure 2.35 Electric potential as a function of excited frequency of four cases [29]

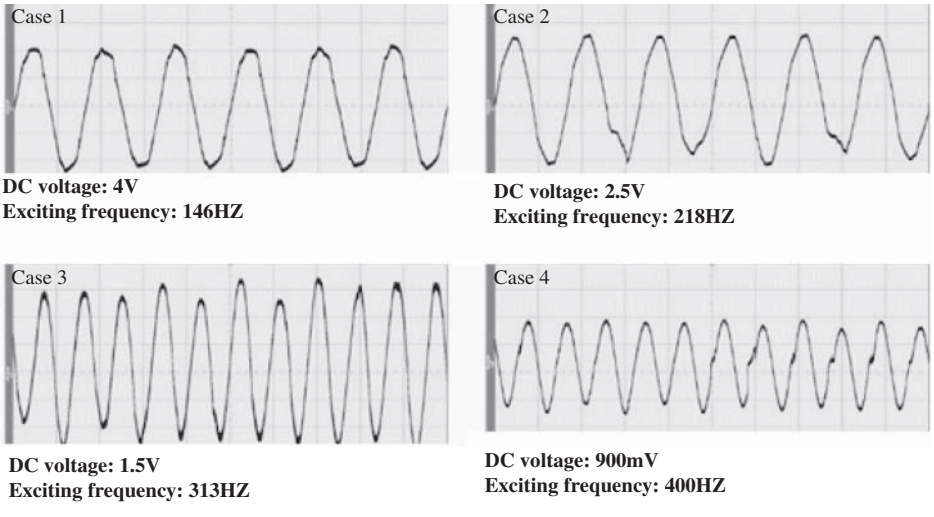

Figure 2.36 (a–d) Resonant frequencies and OCV signals of four cases [29]

Figure 2.35 shows the simulated and the experimental results of electric potential for the four cases. Case 1 has the largest tip deflection and a maximum OCV up to 4 V. The resonant frequency and OCV signal were recorded by the oscillograph, as shown in Figure 2.36.

Table 2.10 lists the experimental results of OCV, CCV, tip deflection, DC voltage across a capacitor, and peak power for the experiment. As described, the bridge rectifier circuit consists of four Schottky diodes with a low forward voltage drop, but

Table 2.10 Peak voltages, tip deflection, peak power, and DC voltages across a capacitor for experiment [28]

Case No.	$\omega_{n(1)}$ (Hz)	U_z (μm)	U_z/u_0	OCV (V)	CCV (V)	Peak power (μW)	DC voltage across a capacitor (V)
Case 1	146	2123.3	64.342	4	3.2	1.247	3.5
Case 2	218	1456.2	44.127	2.5	2.16	0.556	2
Case 3	313	769.4	23.31	1.5	1.08	0.138	1
Case 4	400	454.4	13.769	0.9	0.25	0.007	0.4

the rectifying bridge circuit must consume an electric potential bias of 442 mV. A 0.039 μF storage capacitor is chosen to be a wave filter because it can rapidly recharge. This allows for the largest DC voltage signal to output across this capacitor. The DC voltage of Case 1 across a wave filter after rectification is up to 3.5 V, 2 V for Case 2, 1 V for Case 3, and 0.4 V for Case 4.

The four single harvesters are connected to the different load resistances from 100 kΩ to 10 MΩ. Figure 2.37 shows the variation of load voltage (CCV) and load power with various load resistors for the four cases. The load voltage increases with the resistive load. The results show Case 1 of 3.2 V (Figure 2.37a), Case 2 of 2.16 V (Figure 2.37b), Case 3 of 1.08 V (Figure 2.37c) and Case 4 of 0.25 V at 10 MΩ (Figure 2.37d). The maximum electric power outputs of the four harvesters are 1.247 μW for Case 1, 0.556 μW for Case 2, 0.138 μW for Case 3, and 0.007 μW for Case 4. At a fixed amplitude of shaker vibration, the electric power has a peak value for each case when the load resistance is set at 2 MΩ. The electric potential and power are all proportional to the maximum vertical tip deflection; consequently, they are proportional to the inverse of the damping ratio, as described by Equations (2.19) and (2.22) (refer to Section 2.2.5). The mechanical damping ratio in Cases 3 and 4 therefore increases because of the lower additional mass of the lump structures on the cantilever plate.

The size of a broad bandwidth harvesting system composed of four connected-in-parallel harvesters as an array is 5 cm × 3 cm × 0.8 cm, and all four of the bridge rectifiers have a parallel connection ($B_1 - B_4$). The four electrolytic capacitors (10 μF × 4), connected in parallel ($C_1 - C_4$) as a rechargeable module, were investigated to determine the amount of electric energy that can be harvested at a fixed amplitude of shaker vibration, as shown in Figure 2.38. In addition, the storage gold capacitor (Panasonic 0.022 F/5.5 V) can also be used as a battery to store adequate electric energy stably; however, it requires additional charging time. The four electrolytic capacitors are used because the external flash LED module has a lower forward voltage bias of 1.5–1.55 V and consumes less electrical energy. Figure 2.39 shows an electrical connection of an AC to DC rectification module with a flash LED module. Promising application areas for this design concept of low frequency excitation with broad bandwidth are independent, self-powered devices powered by a varying ambient vibration.

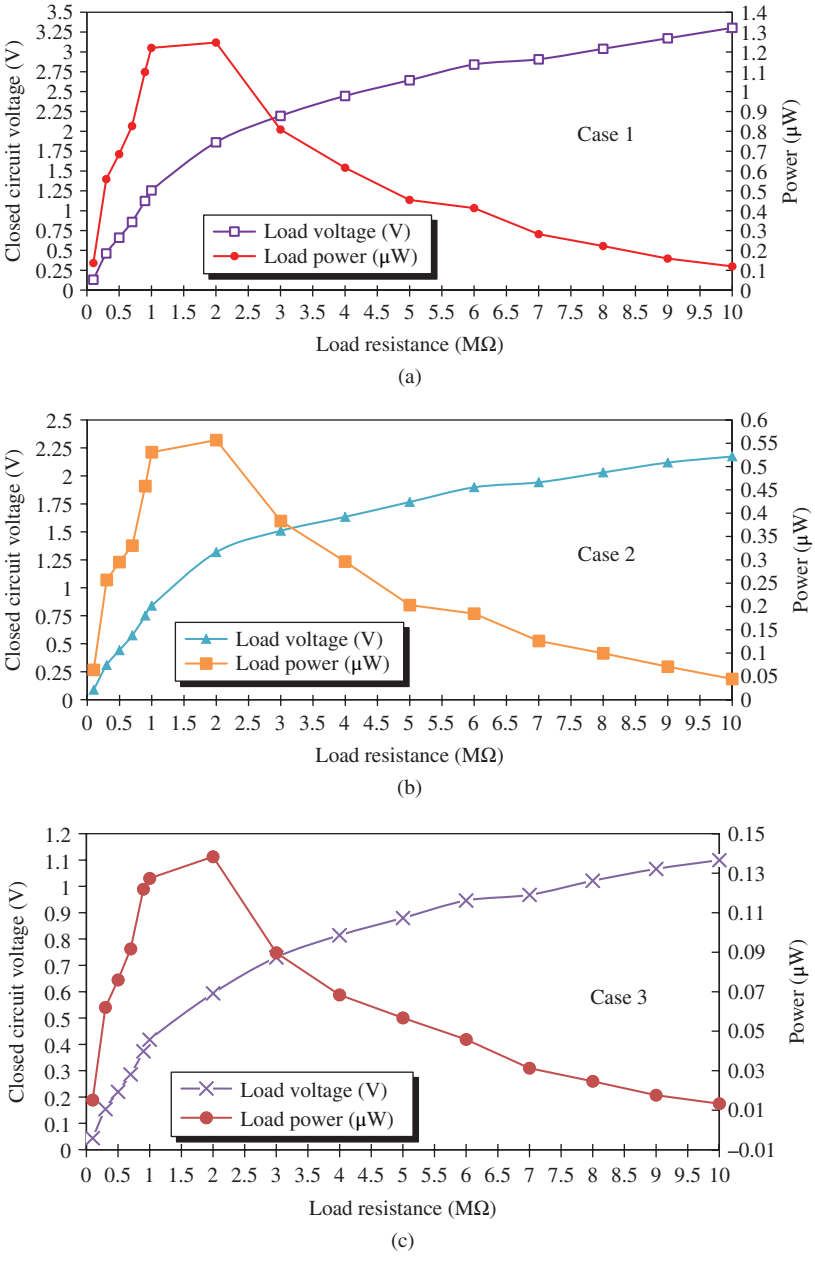

Figure 2.37 Load voltage and load power vs. load resistance of four cases: (a) Case 1 of 3.2 V, (b) Case 2 of 2.16 V, (c) Case 3 of 1.08 V, and (d) Case 4 of 0.25 V at 10 MΩ load [29]

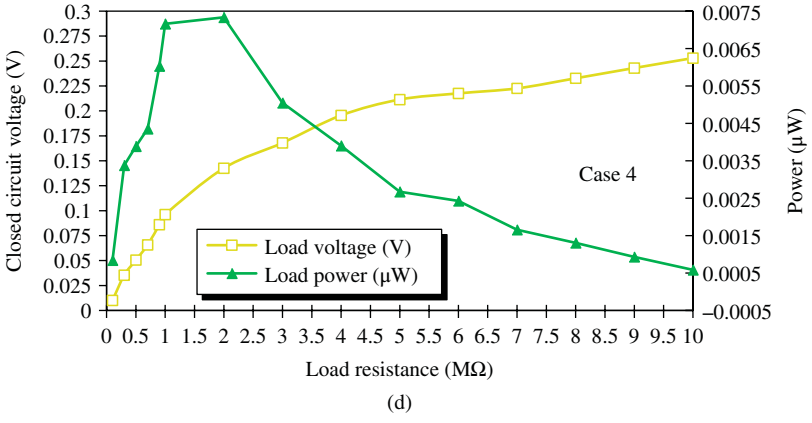

(d)

Figure 2.37 (*continued*)

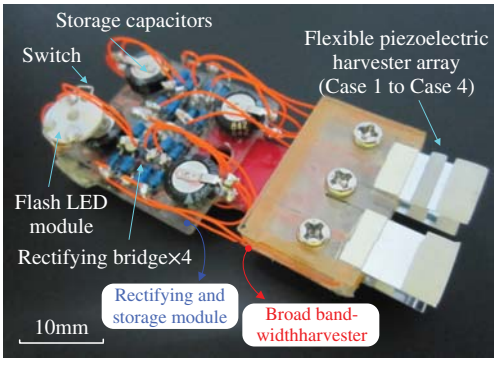

Figure 2.38 The broad bandwidth piezoelectric harvesting system with bridge rectifier circuit and storage module [29]

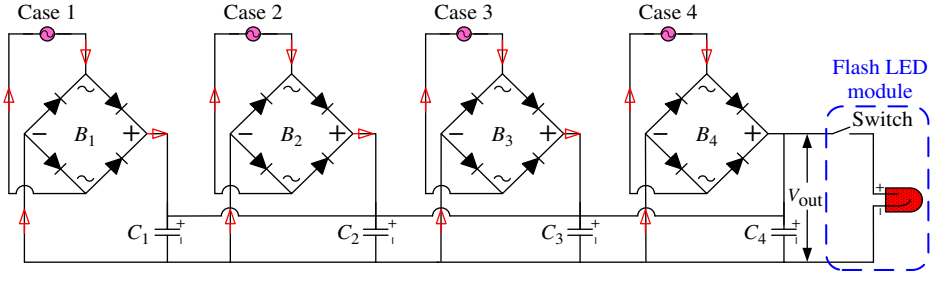

Figure 2.39 AC to DC rectification module with a flash LED module [29]

The system is excited by frequencies ranging from 100 to 400 Hz, as shown in Figure 2.40. First, the broad bandwidth system is directly tested by excitation at 146 Hz. (Case 1 is designed to resonate at 146 Hz.) The amplitude of shaker vibration is set at a fixed amplitude to supply sufficient acceleration for the harvesting system. The result shown in Figure 2.41a was recorded by an oscillograph. The figure shows

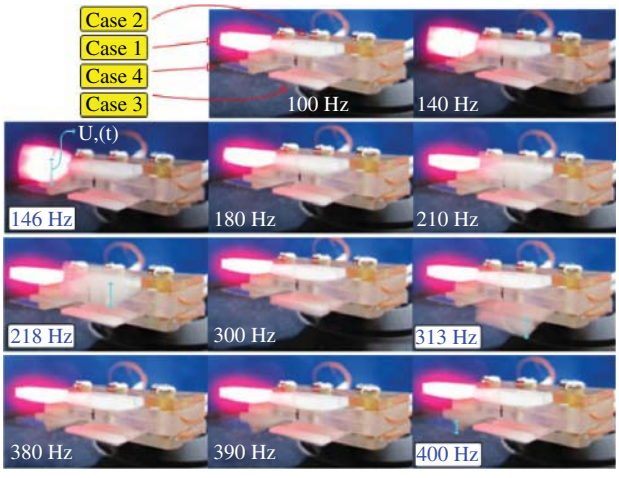

Figure 2.40 The working process of broad bandwidth system with exciting frequency from 100 to 400 Hz [29]

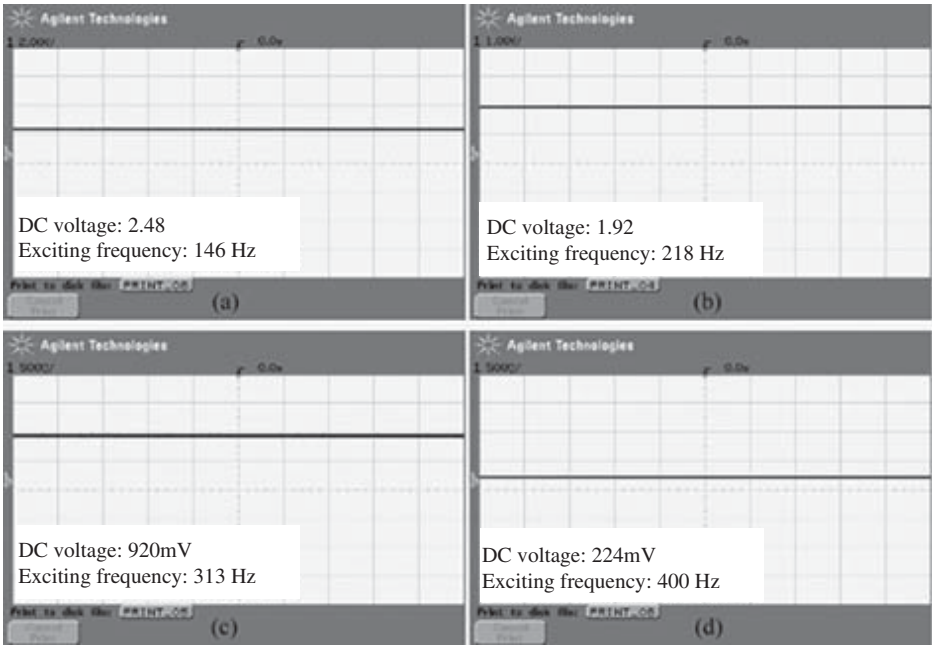

Figure 2.41 DC voltage across a storage module after 60 minutes: (a) harvesting system excited at 146 Hz, (b) 218 Hz, (c) 313 Hz, and (d) 400 Hz [29]

the DC voltage across a storage module after rectification reaches 2.48 V. By contrast, Figure 2.41b–d show the DC voltages for the other three exciting frequencies, 218, 313, and 400 Hz, as well as the DC voltage across a storage module after rectification reaches 1.92 V, 920 mV, and 224 mV, respectively. The charging results of the four cases are shown in Figure 2.42. The storage module can be charged quickly by a full-wave rectified electric potential within 10 minutes. The experimental results of the broad bandwidth system show that the electric power is proportional to the charging time. The charge efficiency of Case 1 is therefore higher than those of the other three cases. When the self-powered harvesting system is running, the storage module can accumulate sufficient electric potential quickly and overcome the forward voltage of the LED module. The LED flashes eight times for 4 s, consuming only approximately 1.1 μJ of electrical energy as shown in Figure 2.43.

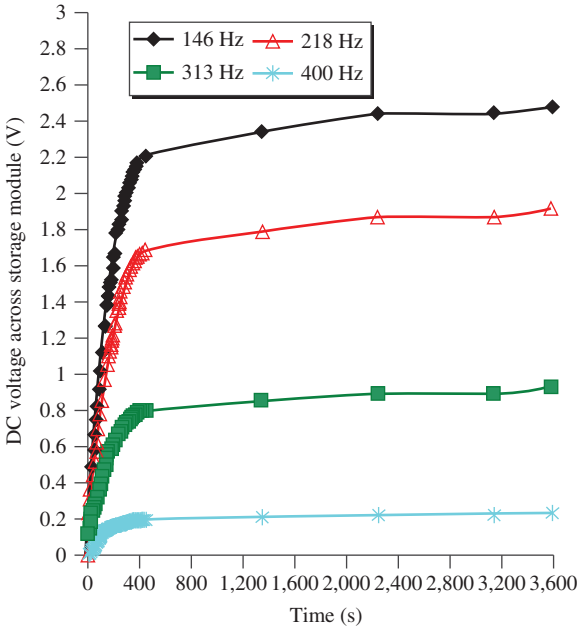

Figure 2.42 Charging results of DC voltage across a storage module when the harvesting system was excited at different operating frequencies [29]

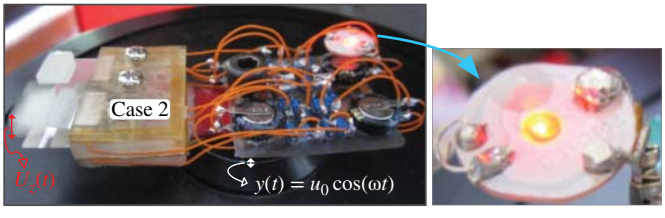

Figure 2.43 The flash LED module driven by the broad bandwidth energy harvester [29]

2.4 Fabrication and Performance of Flexible ZnO/SUS304-Based Piezoelectric Generators

2.4.1 Deposition of Piezoelectric ZnO Thin Films on Stainless Steel Substrates

We now discuss the use of a flexible stainless steel substrate as the bottom electrode for investigating the ZnO-based piezoelectric generator; the substrate is optimal for use because of its flexibility and conductivity. SUS304 has excellent properties such as heat tolerance, anti-corrosion, wear resistance, and mechanical strength. In general, five types of stainless steel substrates have been used in industries, as listed in Table 2.11 [39]. The non-magnetic property is a dominant restricting factor in exploiting microgenerators; the cost is also a considerable obstacle. SUS304 is suitable for use as a substrate in flexible energy generators. Table 2.12 lists the properties and dimensions of SUS304 used in this study.

Table 2.11 The properties of various stainless steel substrates [39]

Type	SUS201	SUS304	SUS309	SUS316	SUS430
Heat resistance	Low	Medium	Medium	High	High
Magnetism	Yes	No	No	No	Yes
Hardness (Brinell hardness)	HB241	HB187	HB187	HB187	HB183
Cost	Low	Low	High	High	Low

Table 2.12 The properties of stainless steel substrates (SUS304) [39]

Young's modulus (Gpa)	130.2
Coefficient of thermal expansion (ppm °C^{-1})	15.3
Thickness (μm)	45
Density (g m^{-3})	7.85
Breadth (cm)	2
Length (cm)	3
Grain coarsening temperature T_g (°C)	>1300

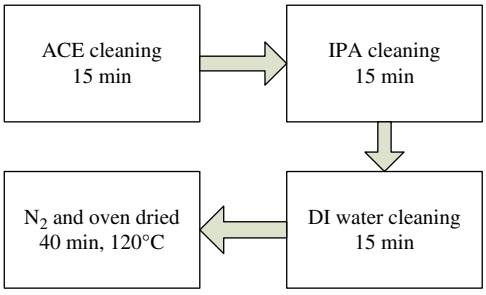

Figure 2.44 The standard spotless cleaning processes

This section introduces the experimental procedures, including the cleaning processes of SUS304, the thin film (electrodes and piezoelectric thin films) depositions using DC/RF sputtering, the optimized sputtering parameters regarding the piezoelectric thin films, the fabrication steps of single-sided and double-sided generators, the analysis of thin films, and the performance of piezoelectric generators.

SUS304 with a thickness of 45 μm was adopted as both flexible substrate and bottom electrode in this study. The substrates were diced into 20 mm × 30 mm pieces and cleaned by conducting the following standard spotless processes to remove the surface contaminants and enhance the adhesion of piezoelectric thin films on substrates. Figure 2.44 schematically depicts the standard spotless cleaning processes. The substrates are cleaned ultrasonically in acetone (ACE), iso-propanol (IPA), and de-ionized (DI) water for 15 minutes each. Finally, the substrates are dried using a nitrogen blow gun and baked for 40 minutes at 120 °C in an oven. After the substrates have been cleaned by the standard spotless cleaning processes, the piezoelectric thin films are deposited.

To deposit piezoelectric ZnO thin films, the RF sputtering system with a 5 cm (2 inch) Zn target is used, and the reactive RF magnetron sputtering method is adopted. The RF sputtering system is equipped with an RF source and a water-cooling pipeline inside to prevent meltdown of the target and demagnetization of the circular magnetic component. The high-purity oxygen (O_2) and argon (Ar) gases of 99.995% are provided as the sputtering gases. The distance between the target and the substrate holder is fixed at 45 mm. The schematic operation procedures are depicted in Figure 2.45.

Another DC sputtering system is adopted to deposit Ti and Pt thin films. This system is equipped with two 2 inch magnetron DC sources with a water-cooling pipeline inside to prevent meltdown of the target and demagnetization of the circular magnetic component. Ti and Pt targets of 99.995% are installed on the two DC guns. The Ar gas of 99.995% purity is provided as the sputtering gas.

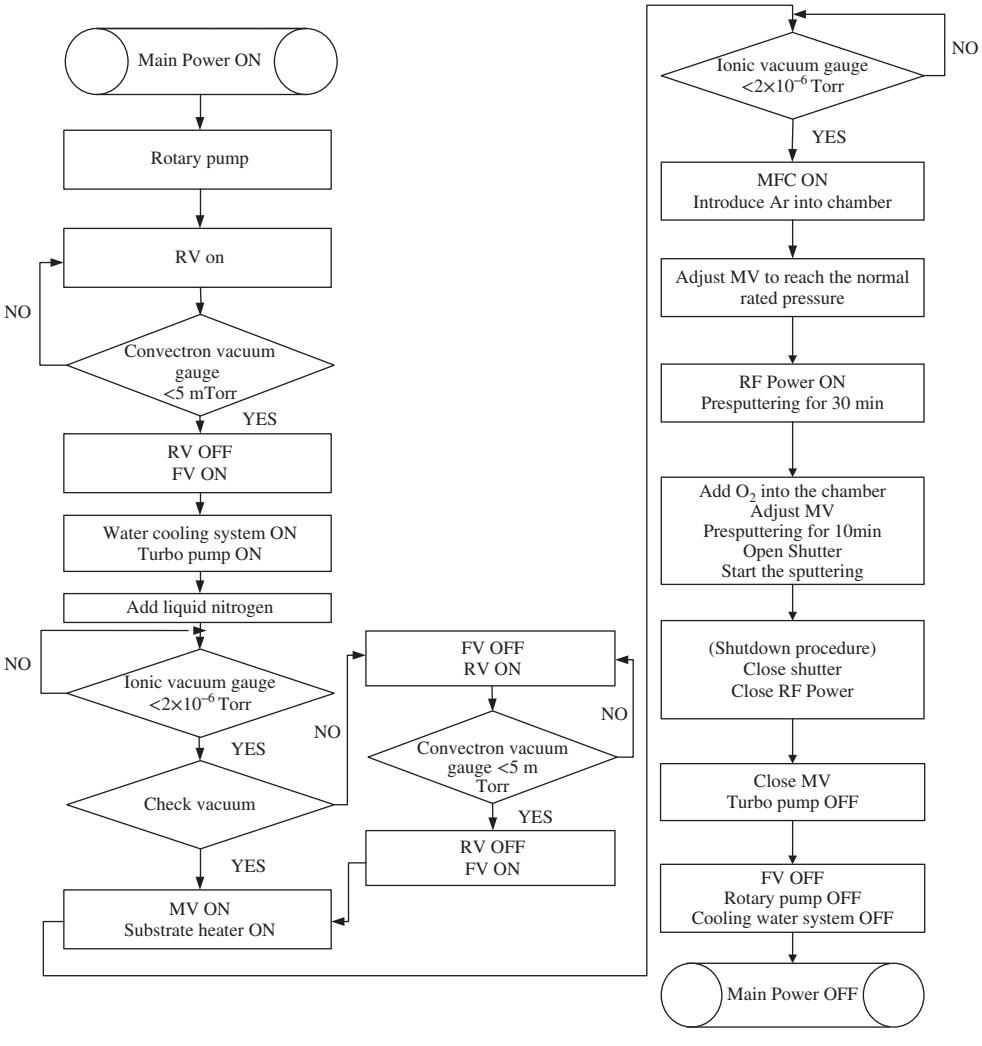

Figure 2.45 Operation procedures of the RF sputtering system

2.4.2 Single-Sided ZnO/SUS304-Based Flexible Piezoelectric Generator

The cleaned SUS304 substrates were adopted as flexible substrates and bottom electrodes. The ZnO piezoelectric thin film was deposited using RF magnetron sputtering with heating at various deposition parameters. Table 2.13 details the sputtering parameters to prepare *c*-axis-oriented piezoelectric ZnO thin films on SUS304 [40].

After the ZnO/SUS304 structure was formed, a copper (Cu) foil was attached to the ZnO/SUS304 as the top electrode of the piezoelectric generator because it has a lower resistivity and is economical. Finally, the electrical properties of the generator (Cu/ZnO/SUS304) were measured using a vibration testing system. To increase

Table 2.13 Deposition parameters of ZnO thin films on SUS304 [40]

Target	Zn (99.995%)				
Base pressure (Torr)	5×10^{-6}				
Substrate-to-target distance (mm)	45				
O_2 concentration ($O_2/O_2 + Ar$, %)	60				
Substrate temperature (°C)	RT	100	200	300	400
Sputtering pressure (mTorr)	3	9	15	21	27
RF power (W)	50	75	100	125	150

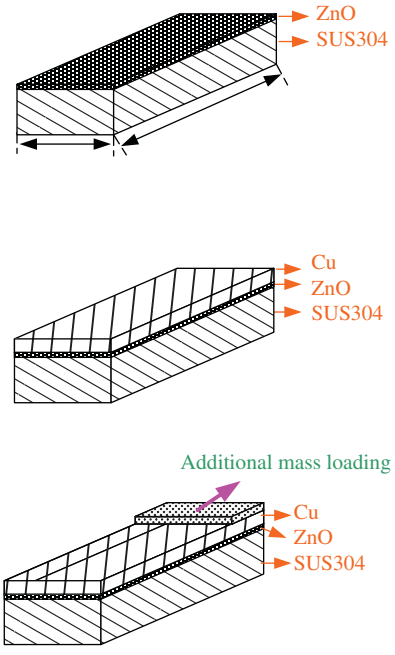

Figure 2.46 (a–c) The fabrication processes of single-sided ZnO/SUS340-based piezoelectric generator [39]

the amplitude of vibration of the generator, an additional mass on the cantilever was attached to the generators. Figure 2.46 depicts the fabrication processes of the device.

2.4.3 Double-Sided ZnO/SUS304-Based Flexible Piezoelectric Generator

After the substrates were cleaned by the standard spotless processes, titanium (Ti) and platinum (Pt) layers were deposited using a dual-gun DC sputtering system on the back side of the SUS304 as a protective layer before depositing the ZnO thin

films. Because the back surface of the SUS304 exhibits a color transition, which is caused by heating at 300 °C during the deposition of the first ZnO layer (front side), the second ZnO layer (back side) does not adhere to the SUS304 unless the Pt/Ti layer is formed.

The front-side and back-side ZnO piezoelectric thin films (1st-ZnO and 2nd-ZnO) were deposited using RF magnetron sputtering with heating. Table 2.14 details the sputtering conditions in preparing first and second *c*-axis-oriented ZnO piezoelectric thin films. After the 1st-ZnO/SUS304/Ti/Pt/2nd-ZnO structure was formed, the Cu foils with low resistivity and low cost were attached to the ZnO surfaces as the top and bottom electrodes. The fabrication steps of a double-sided piezoelectric generator are depicted by Figure 2.47.

The electrical properties of the double-sided piezoelectric generators (Cu/1st-ZnO/SUS304/Ti/Pt/2nd-ZnO/Cu) were measured using a vibration-testing system. For a fixed value of amplitude, the vibration frequency is reduced with the added mass loading. To achieve the designed frequency, the specific mass loading must be attached to the double-sided generator as shown in Figure 2.48.

2.4.4 Characterization of ZnO/SUS304-Based Flexible Piezoelectric Generators

The preferred orientation and crystalline properties of the ZnO thin films were determined by XRD using a Shimadzu XRD-6000 with CuKα radiation. The diffraction angles of ZnO are revealed by scanning between 20° and 60° at a speed of 0.05° per second. The surface morphologies and composition of the thin films were observed by SEM (Philips XL40 FESEM) with an energy-dispersive spectrometer (EDS). The accelerated voltage of the SEM is set at 10 kV, and the magnification is controlled over a range of magnitude from 3000× to 60 000×. The thicknesses of the films were determined using reflectance spectroscopy (Filmetrics F20). Figure 2.49 depicts the vibration-testing system (B&K-LDS V201-PA25E) that was used to measure the electrical properties of the ZnO/SUS304-based piezoelectric generators. The system includes a laser displacement sensor (MEL M72L/4) for measuring the amplitude of vibration.

Table 2.14 Deposition parameters of double-sided ZnO thin films on SUS304 [39]

Target	Substrate-to-target distance (mm)	Base pressure (Torr)	Substrate temperature (°C)	RF power (W)	Sputtering pressure (mTorr)	O_2 concentration ($O_2/O_2 + Ar$, %)
Zn (99.995%)	45	5×10^{-6}	300	75	9	60

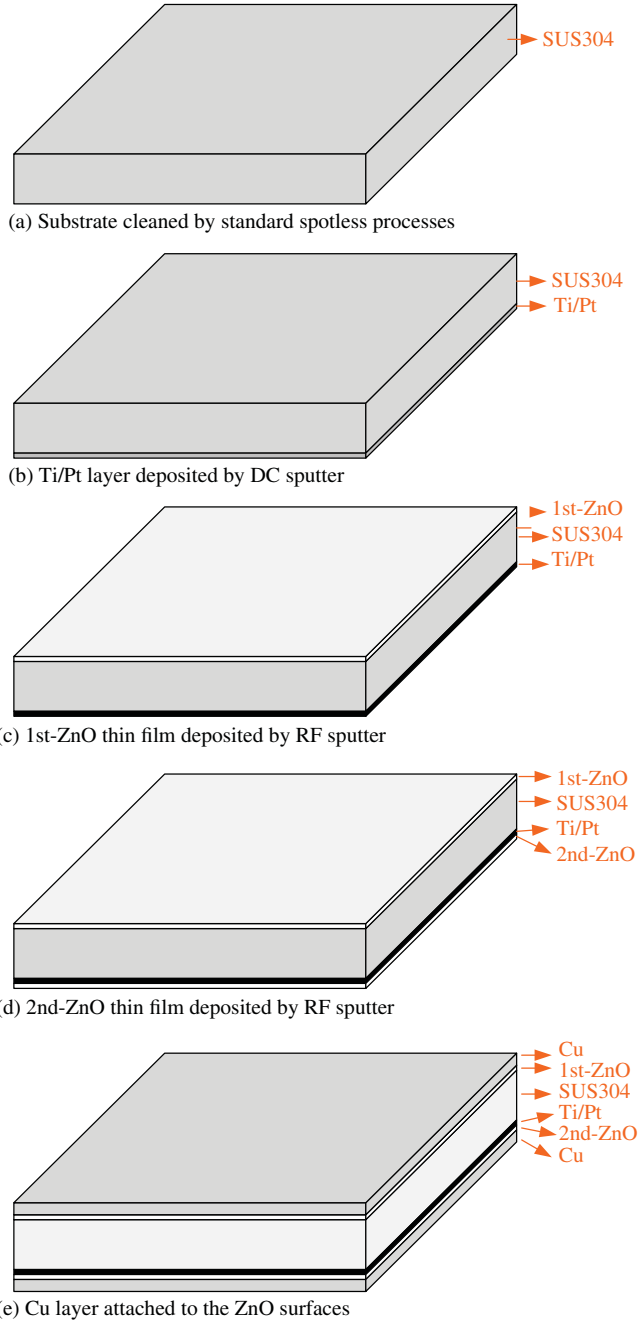

Figure 2.47 (a–e) The fabrication steps of double-sided ZnO/SUS304-based piezoelectric generator

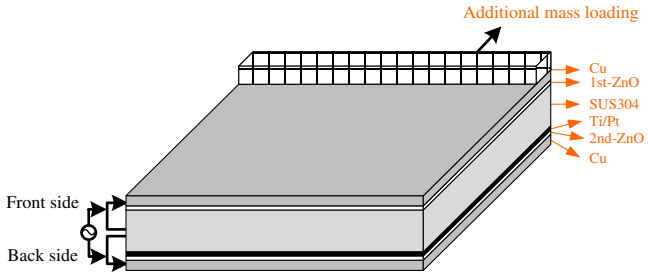

Figure 2.48 The schematic structure of a double-sided ZnO/SUS304-based piezoelectric generator

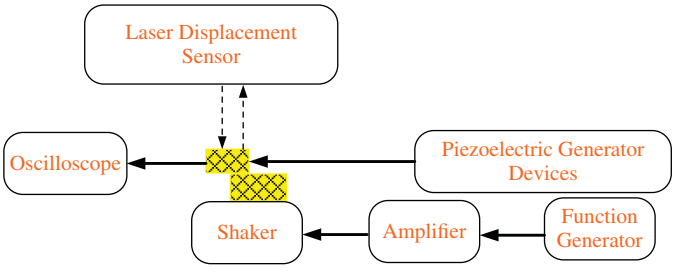

Figure 2.49 The vibration testing system for the ZnO/SUS304-based piezoelectric generators

2.4.5 Structural and Morphological Properties of Piezoelectric ZnO Thin Films on Stainless Steel Substrates

To optimize the piezoelectric characteristics of RF-sputtered ZnO thin films for use in vibration-induced energy generators, various deposition parameters were investigated. The ideal physical properties of piezoelectric films for use in such applications are a strong *c*-axis orientation and a uniform surface structure. In this study, RF power, sputtering pressure, and substrate temperature were controlled to improve the ZnO characteristics. First, the sputtering pressure was controlled to achieve the optimal ZnO layer in a single sputtering process. Because the heating process can improve the piezoelectric properties of ZnO thin films, the substrate temperature was set at 300 °C to investigate the effect of the pressure on ZnO thin films. As shown in Figure 2.50, a sputtering pressure of 9 mTorr resulted in optimal crystallization and a high electromechanical coupling coefficient.

Second, the RF power was controlled, and the substrate temperature was set at 300 °C to investigate the influence of RF power on ZnO thin films. The XRD patterns in Figure 2.51 show that ZnO thin films deposited at 75 W yield a sharp (002) peak with a small FWHM. The RF power was therefore fixed at 75 W to produce a highly textured structure.

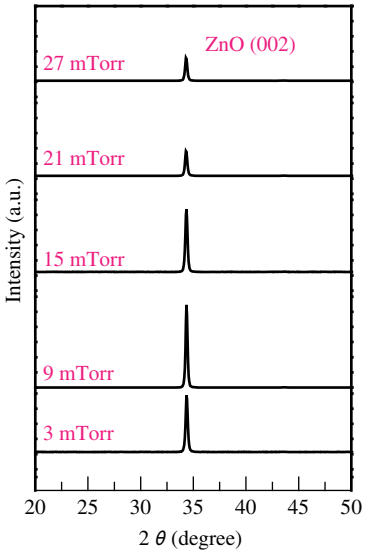

Figure 2.50 The $\theta-2\theta$ X-ray scans of the ZnO thin films deposited under various sputtering pressures. (Fixed sputtering parameters: substrate temperature of 300 °C, RF power of 75 W, O_2 concentration of 60%.)

Third, Figure 2.52 depicts the variation of the XRD patterns of the ZnO thin films deposited on the SUS304 at various substrate temperatures. A sharp (002) peak and narrow FWHM is obtained at substrate temperatures from room temperature (RT) to 300 °C. A stronger XRD intensity indicates that the ZnO thin film has a higher electromechanical coupling coefficient of piezoelectricity. The diffraction angle of ZnO thin films matches that of the standard ZnO films. The internal resistance of the ZnO thin films increased with the piezoelectricity however, as described by Table 2.15 [41].

To select the parameter of the substrate temperature between the piezoelectricity and electricity, four cases of generators were fabricated with ZnO thin films that were deposited at RT, 100, 200, and 300 °C, respectively. The output open voltages of four generators were measured using an electrical property measurement system combined with the vibration-testing system, as shown in Figure 2.49. Table 2.16 shows the OCV ($V_{p\text{-}p}$, peak-to-peak voltage). The OCVs in Generators 1–3 are lower than that in Generator 4. In this study, the substrate temperature was set at 300 °C to ensure the high OCV ($V_{p\text{-}p}$).

Finally, the optimal substrate temperature of 300 °C, RF power of 75 W, and sputtering pressure of 9 mTorr were adopted to deposit piezoelectric ZnO films. The resulting morphologies of ZnO films on the SUS304 appeared dense with smooth surfaces, uniform grain sizes, and strongly textured columnar structures. Hexagonal crystals such as ZnO are believed to exhibit piezoelectricity of unity with a (002)-preferred orientation.

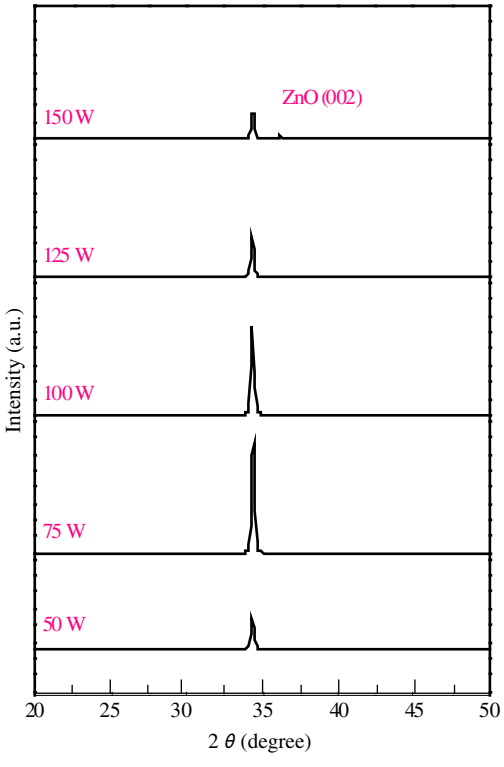

Figure 2.51 The $\theta-2\theta$ X-ray scans of the ZnO thin films deposited under various RF powers. (Fixed sputtering parameters: substrate temperature of 300 °C, sputtering pressure of 9 mTorr, O_2 concentration of 60%.)

2.4.6 Analysis of Adhesion of ZnO Thin Films on Stainless Steel Substrates

In this investigation, a nano-indenter and a nano-scratch tester were applied to determine the mechanical properties of ZnO thin films on stainless steel substrates. Table 2.17 presents the conditions for measuring the mechanical properties of ZnO thin films. The OM images, as shown in Figure 2.53, indicate that the ZnO/SUS304 structure has several favorable properties such as high compressive strength, high fracture strength, and the absence of any breakdown phenomenon. Figure 2.54 presents the scratch depth of the ZnO thin film that was deposited on the SUS304 at various applied stresses. Point A in Figure 2.54 indicates that the ZnO/SUS304 structure endured 500 mN of applied stress without any change to the shape of the surface. Point B in Figure 2.54 shows both the end point and the start point, indicating that no extrusion phenomenon occurs. The ZnO/SUS304-based structure is therefore highly stable and exhibits long-term vibration in natural environments.

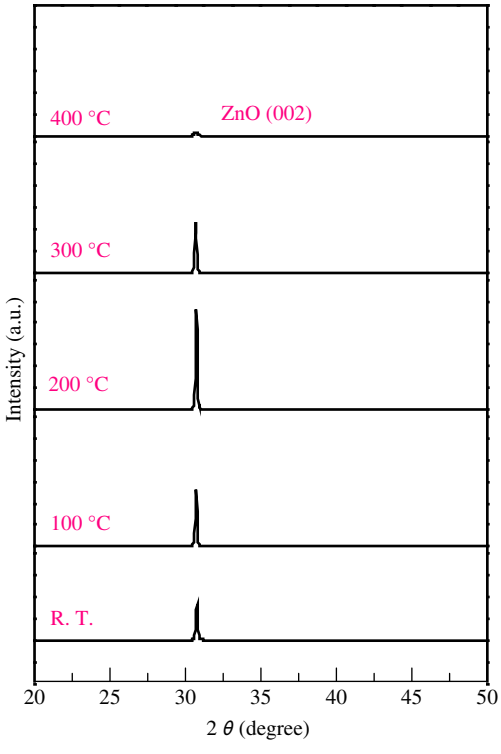

Figure 2.52 The $\theta-2\theta$ X-ray scans of the ZnO thin films deposited under various substrate temperatures. (Fixed sputtering parameters: sputtering pressure of 9 mTorr, RF power of 75 W, O_2 concentration of 60%.)

Table 2.15 The internal resistance of ZnO thin films with various substrate temperatures

Substrate temperature	RT	100 °C	200 °C	300 °C	400 °C
R_{ZnO} (MΩ)	1.254	2.923	5.471	5.120	NA

Table 2.16 The output voltages of four generators [41]

Generator No.	1	2	3	4
Substrate temperature	RT	100 °C	200 °C	300 °C
$V_{p\text{-}p}$ (V)	1.215	1.525	2.687	7.796

Table 2.17 Parameters of the nano-indenter and nano-scratch test

Scratch length (μm)	500
Starting scratch load (mN)	1
Scratch velocity (nm s^{-1})	100
Maximum scratch load (mN)	520
Load applied during profiling (μN)	100
Allowable drift rate (nm s^{-1})	1
Profiling acquisition rate (Hz)	20

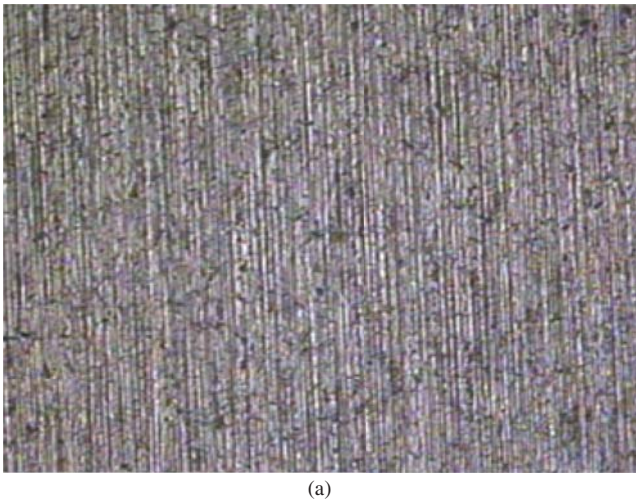

(a)

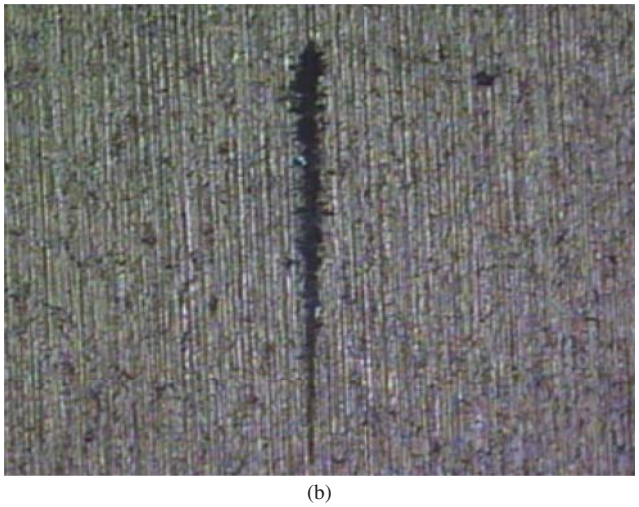

(b)

Figure 2.53 The optical microscopy (OM) drawing of the ZnO thin film on SUS304: (a) the reset condition and (b) after the nano-indenter and nano-scratch test [40]

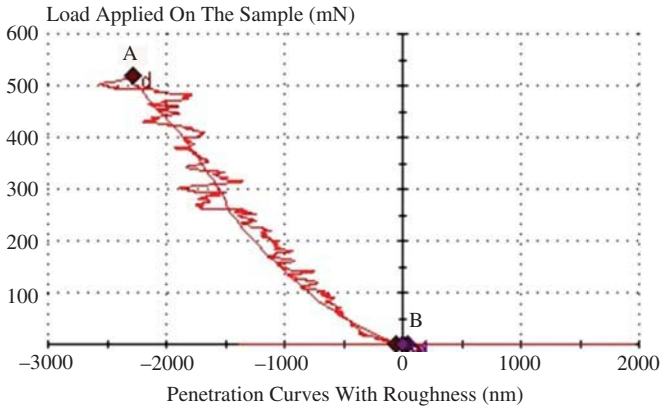

Figure 2.54 The indentation depth variations of the ZnO thin films deposited on the SUS304 with various extra stresses

2.4.7 Electrical Properties of Single-Sided ZnO/SUS304-Based Flexible Piezoelectric Generator

As reported, the excitation frequency and amplitude of vibration critically influence the output voltage of a generator. Figure 2.55 shows the variations of OCV ($V_{p\text{-}p}$) with excitation frequencies at a vibration amplitude of 1 mm. The maximum V_{oc} (open-circuit voltage) of 7.52 V was achieved at an excitation frequency of 75 Hz. Clearly, the ZnO/SUS304-based generator in this study is suitable for low-frequency application. Figure 2.56 shows a plot of the variations of OCV ($V_{p\text{-}p}$) with the amplitude of vibration. The maximum OCV of 10.5 V ($V_{p\text{-}p}$) is reached at a vibration amplitude of 1.19 mm at the vibration frequency of 75 Hz.

The piezoelectric generator can be characterized as high voltage with a low-current output. For applications in this study, the ZnO-based generators were connected to an energy storage or filtering capacitor with a load resistance of 5 MΩ and four Schottky diodes (1N5711) for rectification. The load resistance of 5 MΩ was matched by the internal resistance of the ZnO thin films. Figure 2.57 shows the output DC voltage of 4.64 V, which was rectified by the bridge rectifier circuit and filtered with a 33 nF capacitor at a vibration amplitude of 1.19 mm and a vibration frequency of 75 Hz. As 5 MΩ was loaded, the maximum output DC voltage of 2.24 V and a power output of 1.0 μW cm^{-2} were obtained, thereby demonstrating excellent performance.

To determine the optimal additional mass loading to obtain the higher-power output and lower-vibration frequency, six different mass loadings were added to the single-sided ZnO/SUS304-based generators: 0.05, 0.10, 0.15, 0.30, 0.50, and 0.57 g. The open-circuit output voltages ($V_{p\text{-}p}$) of the six generators were measured, as shown in Table 2.18 [42]. The output voltages in Generators 1, 2, 3, 4, and 6 are lower than

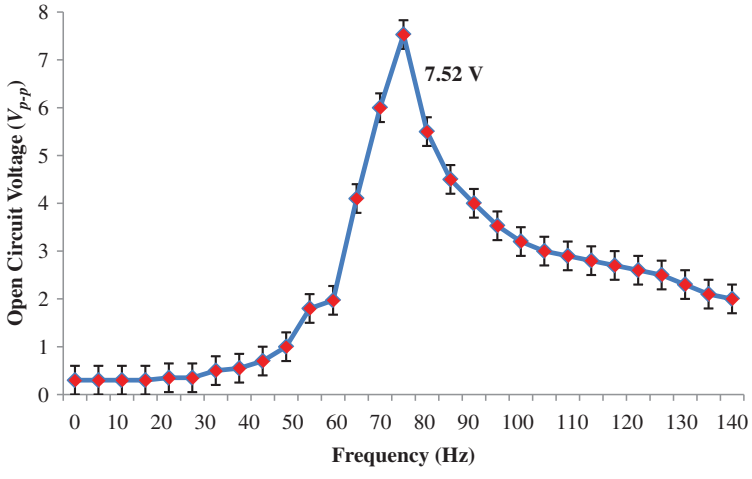

Figure 2.55 Open circuit voltages (OCV, V_{p-p}) with various excitation frequencies (amplitude of vibration: 1 mm)

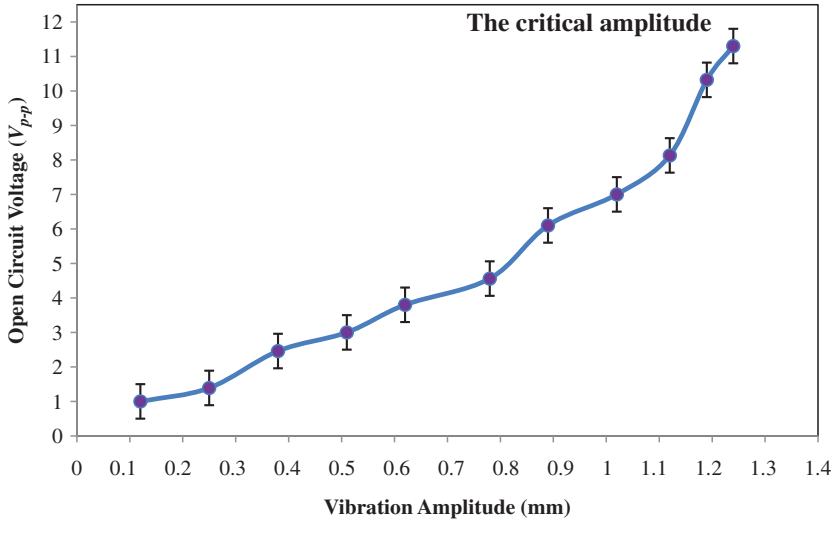

Figure 2.56 The variations of OCV (V_{p-p}) with various vibration amplitudes (vibration frequency: 75 Hz)

that of Generator 5. In this study, the additional mass loading of 0.5 g was adopted to optimize the output voltage. Finally, the maximum OCV (V_{p-p}) of 10.693 V for the single-sided ZnO/SUS304-based generators was reached at the vibration frequency of 82 Hz. Clearly, this single-sided ZnO/SUS304-based generator can be used in vibration-powered applications. Based on these results, a high-performance scheme for designing double-sided generators is warranted.

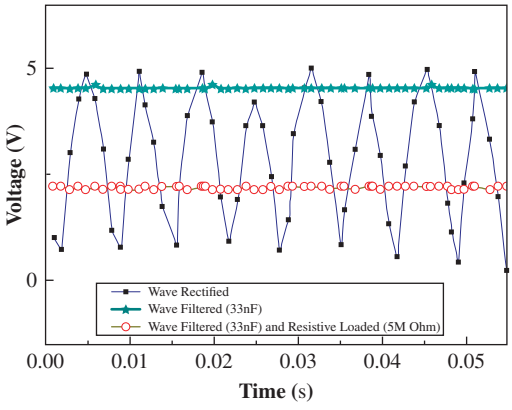

Figure 2.57 The wave forms of various output voltages of optimized piezoelectric generator after rectified, filtered, and resistive loaded

Table 2.18 The output voltages of six generators with various additional mass loading

Generator No.	Additional mass loading (g)	OCV ($V_{p\text{-}p}$)	Vibration frequency (Hz)
1	0.05	1.147	158
2	0.10	2.443	150
3	0.15	3.104	147
4	0.30	5.918	91
5	0.50	10.693	82
6	0.57	10.487	77

2.4.8 Characterization of Double-Sided ZnO/SUS304-Based Flexible Piezoelectric Generator: Analysis and Modification of Back Surface of SUS304

To increase the power output density, the second ZnO piezoelectric thin film should be deposited on the back of the 1st-ZnO/SUS304 directly to form a double-sided generator. However, the results in this study showed that the quality of the second ZnO thin film is poor. The back of the SUS304 exhibited a color transition after heating at 300 °C, and the surface did not favor the growth of the second ZnO layer. Therefore, the back surface before and after 300 °C heating was analyzed using an EDS. Table 2.19 shows how the oxygen content (O_2%) in the back surface of the SUS304 increased considerably after heating at 300 °C.

The results of roughness analyses in Figure 2.58 and Table 2.20 show that, after heating at 300 °C, the surface roughness of the SUS304 increases from 1.455 to 12.592 nm,

Table 2.19 The oxygen contents in the back surface of SUS304 before and after 300 °C heating [39]

Sample No.	O_2 (%) before 300 °C heating	O_2 (%) after 300 °C heating
1	0	14.08
2	4.39	11.73
3	2.42	10.94
4	0	4.89

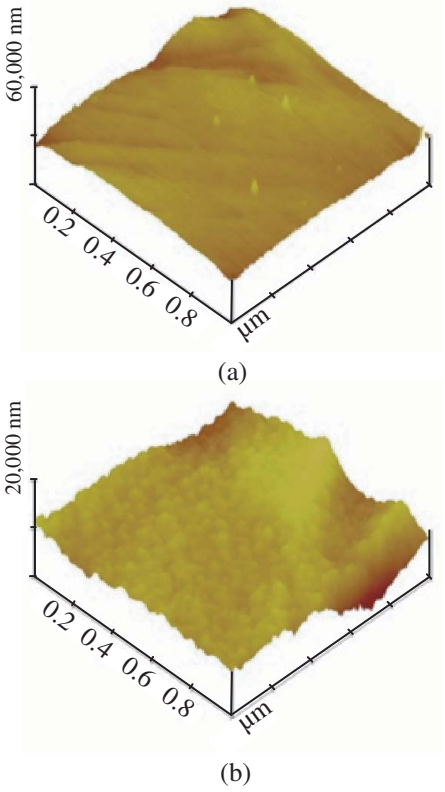

Figure 2.58 Atomic force microscopy (AFM) images of the back surface of SUS304: (a) before and (b) after 300 °C heating [42]

and the second ZnO piezoelectric thin film cannot be deposited on the rough back of the SUS304. To solve this problem, Ti and Pt layers were deposited on the back side of the SUS304 before the first ZnO thin film deposition to improve the adhesion between the second ZnO piezoelectric thin film and the SUS304. Figure 2.59 shows a strong

Table 2.20 The roughness analyses of the back surface of SUS304 before and after 300 °C heating [42]

	Before 300 °C heating	After 300 °C heating
Root mean square roughness R_q (nm)	1.455	12.592
Arithmetic average roughness R_a (nm)	1.075	8.583
Max roughness R_{max} (nm)	26.127	128.03

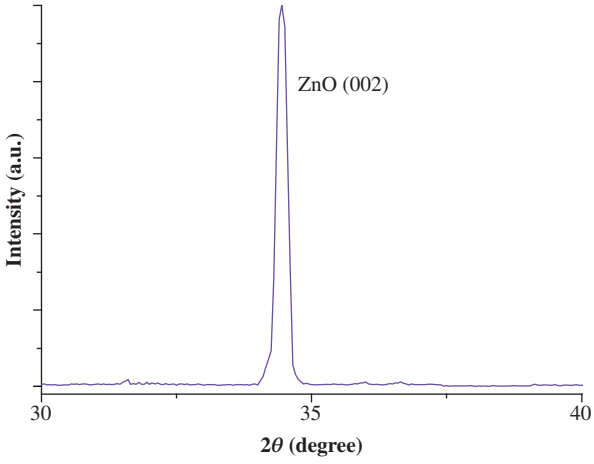

Figure 2.59 The $\theta-2\theta$ X-ray scans of the 2nd-ZnO thin film

(002) peak of the second ZnO layer. In addition, the second ZnO layer exhibits a dense and smooth surface morphology with a highly textured structure, as shown in Figure 2.60. The second ZnO layer deposited on the back of SUS304/Ti/Pt therefore has excellent properties and is effective in double-sided piezoelectric generators.

2.4.9 Electrical Properties of Double-Sided ZnO/SUS304-Based Piezoelectric Generator

Based on previous investigations [43, 44], excitation frequency and amplitude of vibration critically affect the output voltage of a double-sided generator. Figure 2.61 shows a plot of the variation of OCV ($V_{p\text{-}p}$) of a double-sided ZnO/SUS304-based generator at the fixed 1 mm vibration amplitude and various excitation frequencies, in which OCV ($V_{p\text{-}p}$) reached a maximum of 18.2 V at an excitation frequency of 80 Hz.

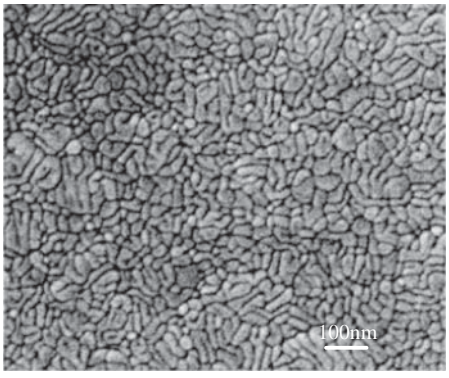

Figure 2.60 The surface morphologies of 2nd-ZnO thin film

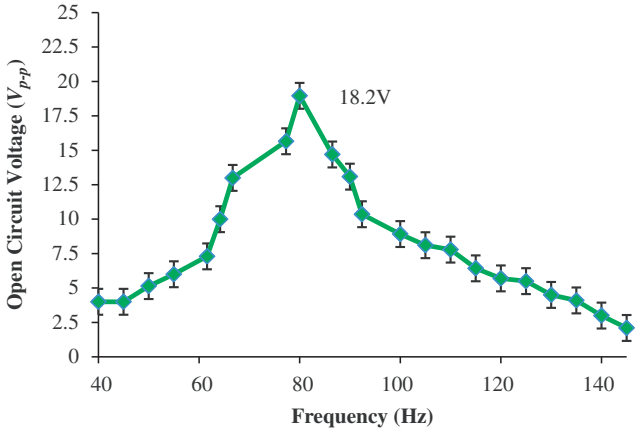

Figure 2.61 The open circuit voltages (V_{p-p}) under various excitation frequencies

Clearly, the double-sided generator used in this study is effective at low-frequency vibration. Figure 2.62 shows a plot of the variation of OCV (V_{p-p}) with the vibration amplitude. The stable value of OCV (V_{p-p}) of 18.2 V is reached at a vibration amplitude of 1 mm and a vibration frequency of 80 Hz. A higher OCV (V_{p-p}) of 20.6 V can be obtained at a higher vibration amplitude; however, the cantilever collapses within a few hours.

In practical applications, double-sided ZnO/SUS304-based generators are rectified using a bridge circuit with four Schottky diodes (1N5711) and filtered using a capacitor of 33 nF. To determine the maximum power extraction, a load resistance of 6 MΩ was used to match the internal resistance of the double-sided ZnO/SUS304-based generator. Figure 2.63 shows the output voltage rectified by the bridge circuit, the voltage that was filtered using a 33 nF capacitor, and the voltage with a resistor of

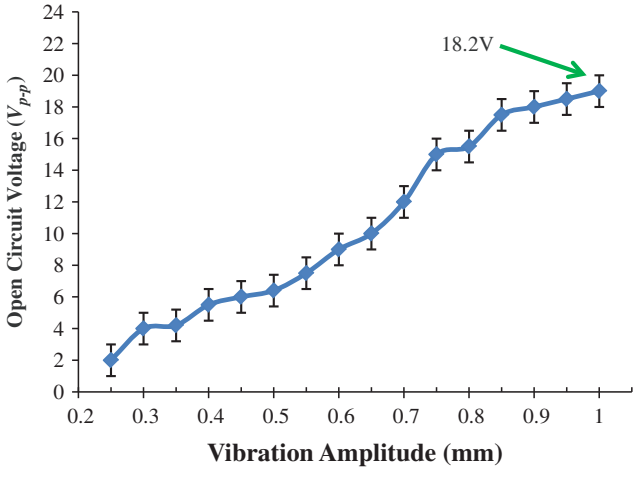

Figure 2.62 The open circuit voltages (V_{p-p}) under various vibration amplitudes

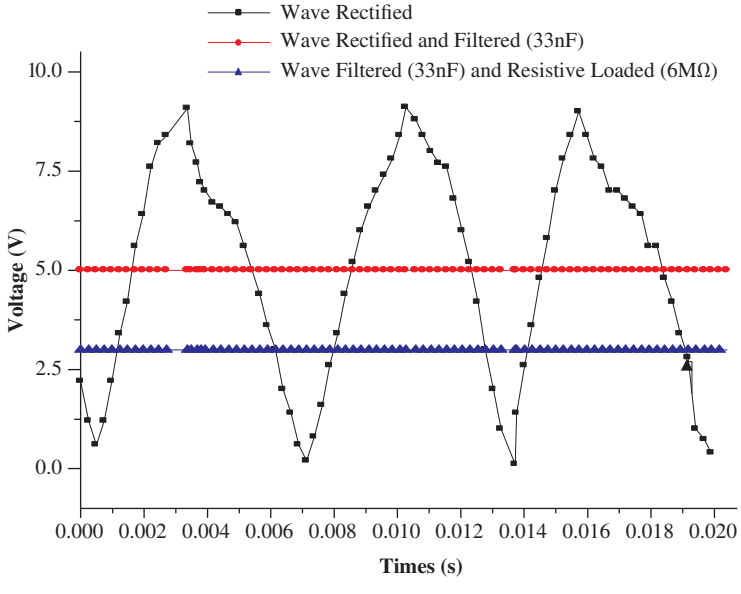

Figure 2.63 The wave forms of output voltages of optimized double-sided ZnO/SUS304-based piezoelectric generator after rectified, filtered, and resistive loaded

6 MΩ loaded, obtained using the optimal generator with vibration amplitude of 1 mm and vibration frequency of 80 Hz.

The maximum DC output voltage with 6 MΩ loading was 2.8 V, and the power output was 1.31 μW cm^{-2}. The variation of the power output ±0.001% was obtained after a continuous 24-hour-long test. To examine the maximum instant power output, a test

with turbulent amplitude of vibration on the piezoelectric generator was conducted. The result shows that the DC output voltage with loading reached a maximum of 4.4 V and a power output of 3.23 $\mu W\,cm^{-2}$.

2.5 Summary

This chapter describes two types of flexible piezoelectric power generators using ZnO piezoelectric thin films. First, a new design of an Al/PET-based flexible energy harvester is proposed. The energy harvester consists of a flexible Al/PET-conductive substrate, piezoelectric ZnO thin film, selectively deposited UV-curable resin lump structures, and a Cu foil electrode. The design and simulation of a piezoelectric cantilever plate is described after using commercial software ANSYS FEA to determine the optimal thickness of the PET substrate, internal stress distribution, operation frequency, and electric potential. Because of the optimal thickness predicted by performing developed accurate, analytical, formulaic analysis, the one-way mechanical strain enhances the induced electric potential can be controlled within the piezoelectric ZnO layer. In addition, the relationship between the model solution of the piezoelectric cantilever plate equation, vibration-induced electric potential, and electric power was determined. ZnO thin film of high (002) *c*-axis-preferred orientation with excellent piezoelectricity was deposited on the Al/PET by using RF magnetron sputtering at room temperature. Al was sputtered on the PET substrate as the bottom electrode because of its low sheet resistance, superior adhesion to PET, and lattice constants matching that of ZnO thin film. The selectively deposited UV-curable resin lump structures as a proof mass were directly constructed on a flexible piezoelectric plate using electrospinning with a stereolithography technique. A single harvester achieves a maximum OCV of 4 V with a power density of 1.247 $\mu W\,cm^{-2}$. This self-powered storage system can drive the warning signal of the LED module under both resonant and non-resonant conditions.

A broad bandwidth harvesting system with an operating frequency range of 100–400 Hz to enhance powering efficiency was also accomplished. This system comprises four units of individual ZnO piezoelectric harvesters in the form of a cantilever structure connected in parallel and a rectifying circuit with a storage module. Comparing the ZnO/Al/PET with the ZnO/ITO/PET structures after the vibration test showed that the adhesion strength of the Al film between the ZnO film and the PET substrate was superior to that of the ITO film. This indicates that Al film provides excellent adhesion between the ZnO thin film and the PET substrate.

The *c*-axis-oriented ZnO thin films were also effectively deposited on flexible stainless steel substrates with particular sputtering parameters to develop another type of piezoelectric generator. The ZnO film not only had a uniform grain size and smooth surface but also a strong *c*-axis orientation and a columnar structure. The strong crystalline properties of thin film contributed substantially to the desired piezoelectricity of the piezoelectric generator. The ZnO/SUS304-based piezoelectric generator provides

a power output of 1.0 $\mu W\,cm^{-2}$. In addition, Ti and Pt layers were deposited using a dual-gun DC sputtering system between the ZnO piezoelectric thin film and the back side of the SUS304 to promote the adhesion between the second ZnO piezoelectric thin film and the SUS304. The second ZnO thin film not only had a uniform grain size and a smooth surface but also a strong *c*-axis orientation and a columnar structure. The double-sided vibration-powered generator therefore provides a smooth and steady power output of 1.3 $\mu W\,cm^{-2}$ and a maximum power output of 3.0 $\mu W\,cm^{-2}$ under turbulent vibration.

References

1. Celso Penche and European (2004) Guide on How to Develop a Small Hydropower Plant, Small Hydropower Association (ESHA).
2. Hatziargyriou, N. and Zervos, A. (2001) Wind power development in Europe. *Proceedings of the IEEE*, **89** (12), 1765–1782.
3. Blunden, L.S. and Bahaj, A.S. (2007) Tidal energy resource assessment for tidal stream generators. *Proceedings of the Institution of Mechanical Engineers, Part A: Journal of Power and Energy*, **221** (2), 137–146.
4. O'Regan, B. and Gratzel, M. (1991) A low-cost, high-efficiency solar cell based on dye-sensitized colloidal TiO_2 films. *Nature*, **353**, 737–740.
5. Green, M.A., Emery, K., King, D.L. *et al*. (2007) Solar cell efficiency tables (Version 29). *Progress in Photovoltaics: Research and Applications*, **15** (1), 35–40.
6. Britt, J. and Ferekides, C. (1993) Thin-film CdS/CdTe solar cell with 15.8% efficiency. *Applied Physics Letters*, **62** (22), 2851–2852.
7. Stephen, N.G. (2006) On energy harvesting from ambient vibration. *Journal of Sound and Vibration*, **293** (1–2), 409–425.
8. Bouendeu, E., Greiner, A., Smith, P.J. and Korvink, J.G. (2011) A low-cost electromagnetic generator for vibration energy harvesting. *IEEE Sensors Journal*, **11** (1), 107–113.
9. Wang, Z.L. (2011) *Nanogenerators for Self-Powered Devices and Systems*, Georgia Institute of Technology, Atlanta, GA.
10. Wang, G.J., Yu, W.C., Lin, Y.H. and Yang, H. (2006) Modeling and fabrication of a piezoelectric vibration-induced micro power generator. *Journal of the Chinese Institute of Chemical Engineers*, **29** (4), 697–706.
11. Williams, C.B. and Yates, R.B. (1996) Analysis of a micro-electric generator for microsystems. *Sensors and Actuators A: Physical*, **52** (1–3), 8–11.
12. Feng, G.H. and Hung, J.C. (2008) Development of wide frequency range-operated micromachined piezoelectric generators based on figure-of-merit analysis. *Microsystem Technologies*, **14** (3), 419–425.
13. Watanabe, S. and Fujiu, T. (1996) PZT thin film actuator/sensor for atomic force microscope. Proceedings of 10th IEEE International Symposium on Applications of Ferroelectrics, vol. 1, pp. 199–204.
14. Jones, P.G., Beeby, S.P. and White, N.M. (2001) Towards a piezoelectric vibration-powered microgenerator. *IEE Proceedings: Science, Measurement & Technology*, **148** (2), 69–72.
15. Roundy, S., Leland, E.S., Baker, J. *et al*. (2005) Improving power output for vibration-based energy scavengers. *Energy Harvesting & Conservation*, **4** (1), 28–36.
16. Fang, H.B., Liu, J.Q., Xu, Z.Y. *et al*. (2006) Fabrication and performance of MEMS-based piezoelectric power generator for vibration energy harvesting. *Microelectronics Journal*, **37** (11), 1280–1284.
17. Minazara, E., Vasic, D., Costa, F. and Poulin, G. (2006) Piezoelectric diaphragm for vibration energy harvesting. *Ultrasonics*, **44** (1), e699–e703.

18. Kulkarni, S., Koukharenko, E., Tudor, J. *et al*. (2007) Fabrication and test of integrated micro-scale vibration based electromagnetic generator. IEEE Solid-State Sensors, Actuators and Microsystems Conference, Lyon, France, 1–14 June, pp. 879–882.
19. O'Donnell, T., Saha, C., Beeby, S. and Tudor, J. (2007) Scaling effects for electromagnetic vibrational power generators. *Microsystem Technologies*, **13** (11–12), 1637–1645.
20. Kulkarni, S., Koukharenko, E., Torah, R. *et al*. (2007) Design, fabrication and test of integrated micro-scale vibration-based electromagnetic generator. *Sensors and Actuators A: Physical*, **145–146**, 336–342.
21. Kim, S.I., Lee, D.H., Lee, Y.P. *et al*. (2008) Low frequency properties of micro power generator using a gold electroplated coil and magnet. *Current Applied Physics*, **8** (2), 138–141.
22. Ma, W., Zhu, R., Rufer, L. *et al*. (2007) An integrated floating-electrode electric microgenerator. *IEEE Journal of Microelectromechanical Systems*, **16** (1), 29–37.
23. Serre, C., Pérez-Rodríguez, A., Fondevilla, N. *et al*. (2007) Design and implementation of mechanical resonators for optimized inertial electromagnetic microgenerators. *Microsystem Technologies*, **14** (4–5), 653–658.
24. Giordano, C., Ingrosso, I., Todaro, M.T. *et al*. (2009) AlN on polysilicon piezoelectric cantilevers for sensors/actuators. *Microelectronic Engineering*, **86** (4), 1204–1207.
25. Chen, P.H. and Lin, S.C. (2007) Wind-powered piezo generators. The 33rd Annual Conference of the IEEE Industrial Electronics Society (IECON), Taipei, Taiwan, pp. 2163–2168.
26. Liu, J.Q., Fang, H.B., Xu, Z.Y. *et al*. (2008) A MEMS-based piezoelectric power generator array for vibration energy harvesting. *Microelectronics Journal*, **39** (5), 802–806.
27. Dutoit, N.E., Wardle, B.L. and Kim, S.G. (2005) Design considerations for MEMS-scale piezoelectric mechanical vibration energy harvesters. *Integrated Ferroelectrics*, vol. **71**(1), Taylor & Francis, pp. 121–160.
28. Liu, Z.H. (2012) Design and fabrication of flexible piezoelectric harvesters based on ZnO thin films and PVDF nanofibers. PhD thesis, National Sun Yat-Sen University, Kaohsiung, Taiwan.
29. Pan, C.T., Liu, Z.H. and Chen, Y.C. (2012) Study of broad bandwidth vibrational energy harvesting system with optimum thickness of PET substrate. *Current Applied Physics*, **12** (3), 684–696.
30. Yang, R., Qin, Y., Dai, L. and Wang, Z.L. (2009) Power generation with laterally packaged piezoelectric fine wires. *Nature Nanotechnology*, **4** (1), 34–39.
31. Bien, D.C. S., Mitchell, N.S. J. and Gamble, H.S. (2006) *Micro-Machined Passive Valves: Fabrication Techniques, Characterisation and Their Application*. Springer, pp. 741–800.
32. Lu, F., Lee, H.P. and Lim, S.P. (2004) Modeling and analysis of micro piezoelectric power generators for micro-electromechanical-systems applications. *Smart Materials and Structures*, **13** (1), 57–63.
33. Ugural, A.C. (1999) *Stresses in Plates and Shells*, 2nd edn, McGraw-Hill, New York.
34. Detwiler, D.T., Shen, M.-H.H. and Venkayya, V.B. (1995) Finite element analysis of laminated composite structures containing distributed piezoelectric actuators and sensors. *Finite Elements in Analysis and Design*, **20** (2), 87–100.
35. Hwang, W.S. and Park, H.C. (1993) Finite element modeling of piezoelectric sensors and actuators. *American Institute of Aeronautics and Astronautics*, **31** (5), 930–937.
36. Sohn, J.W., Choi, S.B. and Lee, D.Y. (2005) An investigation on piezoelectric energy harvesting for MEMS power sources. *Journal of Mechanical Engineering Science*, **219** (4), 429–436.
37. Chen, S.N., Wang, G.J. and Chien, M.C. (2006) Analytical modeling of piezoelectric vibration-induced micro power generator. *Mechatronics*, **16** (7), 379–387.
38. Changand, M.Y. and Kuo, J.J. (2004) *The Study of Deposited ITO Films On Flexible Substrates by R.F. Sputtering Technology At Room Temperature*, Taiwan Photonics Society.
39. Chang, W.T., Chen, Y.C., Kao, K.S. *et al*. (2012) Design and fabrication of a double-sided piezoelectric transducer for harvesting vibration power. *Thin Solid Films*, **529**, 39–44.

40. Chang, W.T., Chen, Y.C., Lin, R.C. *et al*. (2011) Wind-power generators based on ZnO piezoelectric thin films on stainless steel substrates. *Current Applied Physics*, **11** (1), S333–S338.
41. Huang, Y.-C. (2009) Investigation of ZnO thin films deposited on stainless steel substrates for piezoelectric transducers application. MSc thesis, National Sun Yat-Sen University, Kaohsiung, Taiwan.
42. Chu, Y.-H. (2010) Study of double-sided ZnO piezoelectric transducer. MSc thesis, National Sun Yat-Sen University, Kaohsiung, Taiwan.
43. Taha, L.Y., Majlis, B.Y., and Al Ali, A. (2006) Modelling and analysis of a transformer based MEMS piezoelectric vibration type microgenerator. IEEE International Conference on Semiconductor Electronics, ICSE, pp. 294–298.
44. Mehraeen, S., Jagannathan, S. and Corzine, K.A. (2010) Energy harvesting from vibration with alternate scavenging circuitry and tapered cantilever beam. *IEEE Transactions on Industrial Electronics*, **57** (3), 820–830.